
Universidade de Aveiro Departamento de Física
2010

Inês Monteiro de Sena Silvares de Carvalho

Caracterização estrutural e magnética de filmes finos de $LaBaMnO_3$

Structural and magnetic characterization of $LaBaMnO_3$ thin films

Universidade de Aveiro Departamento de Física
2010

Inês Monteiro de Sena Silvares de Carvalho

Caracterização estrutural e magnética de filmes finos de $LaBaMnO_3$

Dissertação apresentada à Universidade de Aveiro para cumprimento dos requisitos necessários à obtenção do grau de Mestre em Engenharia Física, realizada sob a orientação científica do Dr. Vítor Amaral, Professor Catedrático do Departamento de Física da Universidade de Aveiro, e do Dr. Armando Lourenço, Professor Auxiliar do Departamento de Física da Universidade de Aveiro

o júri

presidente

Prof. Doutor João de Lemos Pinto
professor catedrático do Departamento de Física da Universidade de Aveiro

Prof. Doutor Pedro Manuel de Melo Bandeira Tavares
professor associado do Departamento de Química da Universidade de Trás-os-Montes e Alto Douro, Vila Real

Prof. Doutor Vítor Brás de Sequeira Amaral
professor catedrático do Departamento de Física da Universidade de Aveiro

Prof. Doutor Armando António Cardoso dos Santos Lourenço
professor auxiliar do Departamento de Física da Universidade de Aveiro

acknowledgements

I'll start by thanking both my supervisors, Professor Vitor Amaral and Professor Armando Lourenço for giving me the opportunity to perform this work and for all their teachings. I would also like to thank to Dra. Rosário Soares, Narciso Soares and Soma Das for their patience, kindness and help during all this work and to Professora Margarida Cruz for giving me the opportunity to do magnetic measurements at her laboratory.
Finally, I would like to address special thanks to family and my friends Cátia, Jennifer, Menno, João, Carlos and João.
Thank you.

keywords Thin films, $LaBaMnO_3$, Al_2O_3, MgO, different thickness, rhomboedric, cubic, ferromagnetism

abstract

This work focuses on a comparison between $LaBaMnO_3$ thin films grown by sputtering on two different substrates: Al_2O_3 and MgO. 3 sputtering depositions were preformed for each substrate each with a different deposition time, leading to different thicknesses from 10 nm to 70 nm.

For Al_2O_3 substrate films a rhomboedric structure is observed and the material has grown according to the sapphire substrate. Magnetization analysis leads to the conclusion that ferromagnetism is still observed at RT and reasons for that to happen are suggested, one being the possibility that the thin film is not homogeneous. Electric measurements show a transition from metallic to insulator behavior from 220 to 240K.

MgO substrate thin films structure analysis shows that peaks grow larger as thickness increases inducing the idea of interdiffusions in the interface that alter the crystallographic quality of the films. Compared to the sapphire substrate thin films, these samples show a much lower ferromagnetic order at RT and magnetization as a function of temperature lead to the possibility of a second T_C.

palavras-chave

Filmes finos, $LaBaMnO_3$, Al_2O_3, MgO, espessuras diferentes, romboédrico, cubico, ferromagnetismo

resumo

Com o presente trabalho pretende-se efectuar uma comparação entre filmes finos de $LaBaMnO_3$ crescidos por sputtering em substratos de Al_2O_3 e MgO. 3 deposições foram efectuadas com variação do tempo de deposição, originado espessuras entre 10 e 70 nm.

Filmes crescidos no substrato Al_2O_3 apresentam uma estrutura romboedrica, tendo crescido de acordo com o substrato de safira. A análise de magnetização permite concluir que existe ferromagnetismo à temperatura ambiente e razões para tal são sugeridas, entre as quais a possibilidade de filmes não homogéneos. As medidas electricas demonstram uma transição metal-isolador a temperaturas entre 220 e 240K.

A análise estrutural efectuada a filmes finos de MgO evidencia um alargamento dos picos com o aumento da espessura induzindo a ideia de interdifusões na interface que alterem a qualidade cristalográfica dos filmes. O ordenamento ferromagnetico evidenciado à temperatura ambiente é inferior ao dos flimes crescidos em safira e os valores obtidos de magnetização em função da temperatura sugerem uma possivel segunda T_C.

Contents

Index of Figures

Index of Tables

1 Manganites

The crystallographic structure of manganites was first studied in the decade of 1950, by Jonker and Van Santer. The designation manganite was proposed by these authors and refers to materials with the chemical formula $R_{1-x}A_xMnO_3$. R represents a trivalent rare-earth and A refers to a divalent cation such as Ca, Sr, Ba, Pb.

1.1 Ideal Crystallographic structure

Manganites have an ideal crystallographic cubic system of ABO_3 *Pm3m* space group, also known as perovskite (Gustav Rose, 1939). This structure can be understood as a face-centered cubic (fcc) and is formed by O^{2-} anions, an A cation and a small B cation in the centre of the cube. This last cation, B, is surrounded by octahedral oxygen [Figure 1].

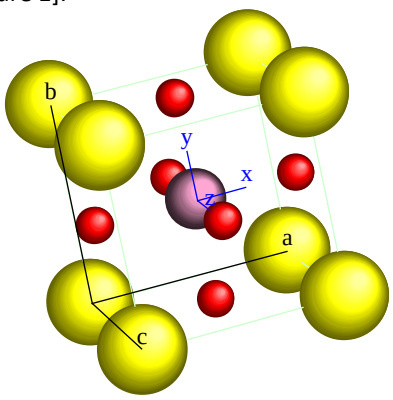

Figure 1 – Manganites ideal crystallographic structure.

1.2 Structural Distortions

1.2.1 Tolerance Factor

Perovskite-type structures can stabilize in distorted symmetries such as orthorhombic, rhomboedric or tetragonal. The stabilization of the structure is determined by the tolerance factor that depends on the A and B ionic radius, r_A and r_B, and on the oxygen ionic radius, r_O.

$$t = \frac{r_A + r_O}{\sqrt{r_B + r_O}} \quad (1)$$

In the ideal cubic perovskite structure, $t = 1$. However, as the value differs from 1 internal stress increases and the cubic lattice becomes unstable.

When A ions are too small to fill the space in the cube centre, the oxygen tend to move toward that centre and the value r_A+r_O is reduced [1]. At $t < 1$, (B - O) bonds are under tension and (A - O) bonds under compression. The induced stress is alleviated by a cooperative rotation of MnO_3 octahedron that lowers the space symmetry from cubic. At this state three different rotations may happen: from a cubic [001] axis to tetragonal, from a cubic [111] axis to rhombohedral or from a cubic [110] axis to orthorhombic [2].

A $t > 1$ the structure of the cell changes from cubic to orthorhombic or rhombohedral.

1.2.2 Crystal field and Jahn-Teller effect

3d valence electrons in transition metals have five degenerate orbital states available: d_{xy}, d_{zx}, d_{yz}, $d_{x^2-y^2}$, d_{z^2}. For 2p electrons in oxygen three degenerate orbitals appear: p_x, p_y, p_z.

Still, in the case of manganites the d orbitals of the transitions metal ions $Mn^{3+}(3d^4)$ and $Mn^{4+}(3d^3)$ located at the centre of the oxygen octahedral O^{2-} $(2p^6)$ are no longer degenerate.

The $d_{x^2-y^2}$ and the d_{z^2} are directed towards the O^{2-} neighbour atoms while the other three orbitals have their lobes oriented between the oxygen but due to Coulombian repulsion caused by the oxygen on the manganese, the first two orbitals are not as energetically favourable as d_{xy}, d_{zx} and d_{yz} and the degeneracy is lifted, forming two new groups with different energy. One group with the orbitals $d_{x^2-z^2}$ and d_{z^2} and an energy of $^{3\Delta}/_{5}$ higher than the free ions (known as e_g), and another group with the d_{xy}, d_{zx} and d_{yz} orbitals that has a $^{2\Delta}/_{5}$ energy lower than the free ions (known as t_{2g}).

The energy difference between the two groups, Δ, is called crystal field splitting and has a value of approximately 1,5 eV for manganites.

Furthermore, if the ion is $Mn^{3+}(3d^4)$ three electrons are located in the t_{2g} orbitals and the fourth is at the e_g orbitals. According to Hund's rules, the electrons have parallels spins and a high energy is required to put the electron from the e_g orbital at the high energy orbitals. In order for this to be possible, the octahedral deforms. Figure 2 represents the level splitting for Mn^{3+}.

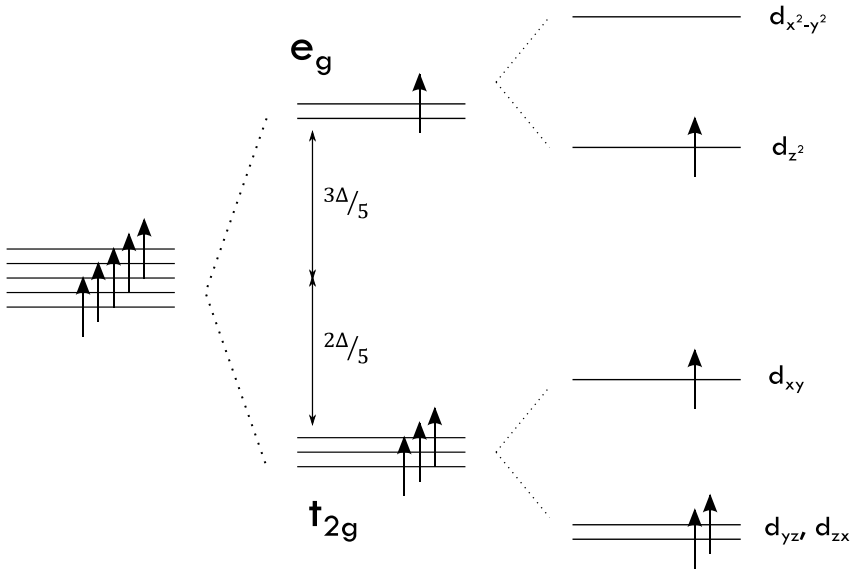

Figure 2 - Field splitting of the five-fold degenerated atomic 3d levels into lower t_{2g} and higher e_g levels.

1.3 Doping with Barium

When doped with Barium, the Lanthanum manganite $LaMnO_3$ suffers a chemical substitution of La ions for Ba ions. However, since Lanthanum is a trivalent ion and Barium is divalent (La^{3+}, Ba^{2+}), the substitution leads to the change of some of the manganese ion valence from Mn^{3+} to Mn^{4+} [2]. The resulting crystal is mixed-valent $La_{1-x}Ba_xMnO_3$, where x is the percentage of doping. The Ba and La are randomly occupying the A sites of perovskite-type structure. Similar situations also occur for doping with Ca^{2+} or Sr^{2+}.

The level of dopage changes the type of crystal cell that is formed.

The ration Mn^{3+}/Mn^{4+} is a key component for understanding the magnetic and transport properties. A higher percentage of Mn^{4+} (which implies a higher doping level) can lead to an increase in the oxygen content and the formula can be written $La_{1-x}Ba_xMnO_{3+\delta}$, where δ is the excess oxygen and depends on the preparation/heat treatment conditions [3].

$La_{1-x}Ba_xMnO_3$	x = 0	x = 0.2	x = 0.3	x = 0.5
Space group	Pnma (62)	R3c (167)	R3c (167)	Pm3m (221)
Crystal structure	Orthorhombic	Rhombohedral	Rhombohedral	Cubic
Parameters	a = 5.536(7) b = 7.692(9) c = 5.747(3)	a = 5.556(2) c = 13.470(8)	a = 5.539(3) c = 13.504(6)	a = 3.908(1)
Mn	½ ½ ½	0 0 0	0 0 0	½ ½ ½
La/Ba	0 0 0	0 0 ¼	0 0 ¼	0 0 0
O	½ ½ 0	0.454(3) 0 ¼	0.468(1) 0 ¼	½ ½ 0

Table 1 - Space groups, cell parameters and atomic positions for different levels of dopage [4], [5] (at room temperature). Other crystal structures are found in the literature.

1.4 Magnetic Characteristics

Depending on the chemical elements used, compounds with the system ABO_3 (B=Mn) show a variety of magnetic and electric phenomena, including ferromagnetic (FM) and antiferromagnetic (AF) ordering [2].

$LaMnO_3$ is an AF insulator [1] due to the presence of only Mn^{3+} ions that couple antiferromagnetically through super exchange interactions.

On the other hand, when doped with divalent ions the Mn^{4+} ions created to balance the charge deficit change the material magnetic characteristics to FM, exhibiting an electrical change from insulator (I) to metal (M) [4], [6]. The compound $La_{1-x}Ba_xMnO_3$ becomes a FM metallic and changes to paramagnetic (P) insulator, above Curie temperature ($T_C \sim 325\ K$ for x=0.2) [7], [8].

It is observed that for $(La^{3+}Mn^{3+}O_3^{2-})_{1-x}(Ba^{2+}Mn^{4+}O_3^{2-})_x$ with x=0.2, used in this work, the low temperature ferromagnetic state is metallic whereas the high-temperature paramagnetic state is electrically insulating [9].

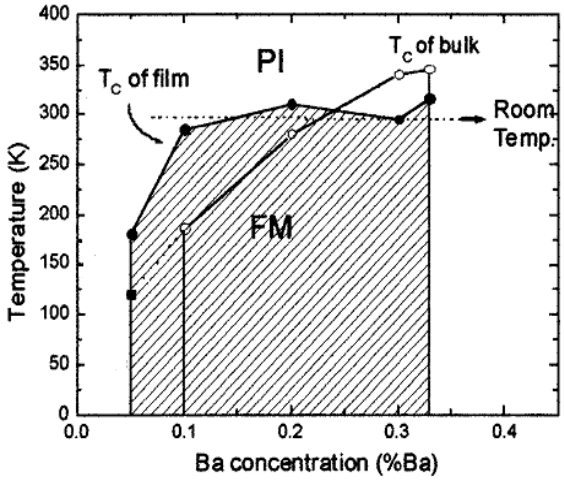

Figure 3 - Phase diagram of LBM thin films with 20 nm thickness and comparison with bulk. Adapted from [8].

Jun Zhang *et al.* studied the strain effect and phase diagram of $LaBaMnO_3/SrTiO_3$[1] thin films, with $0{,}05 \leq x \leq 0{,}33$, concluding that tensile strained thin films with lower doping levels ($x = 0{,}1 - 0{,}2$) show a higher T_C when compared to doping levels of $x = 0{,}3$ or $x = 0{,}33$, being $T_C = 310\ K$ for a thin film with $x = 0{,}2$. Also, it is established that, when compared with bulk compounds with the same doping level, the

[1] $SrTiO_3$ has a cubic crystallographic structure such as MgO, one of the substrates used for this work.

ferromagnetism of LaBaMnO3 is suppressed in compressive strain - $x = 0{,}3 - 0{,}33$ - and enhanced in tensile strain - $x = 0{,}05 - 0{,}2$ [8]. The phase diagram is shown in Figure 3.

Some representative values of temperature dependence of magnetization for bulks and thin films are presented in Figure 4.

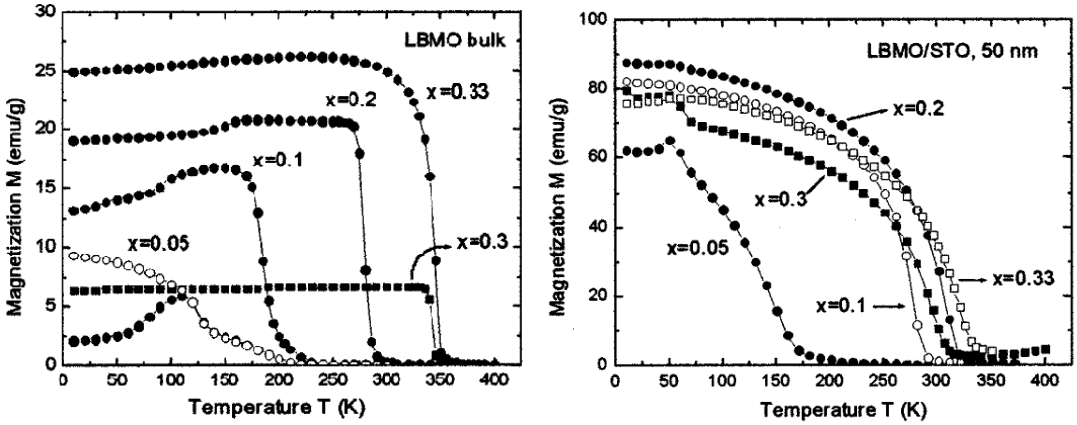

Figure 4 - Magnetization values of $LaBaMnO_3/SrTiO_3$. On the left: bulk values. On the right: thin film with 50 nm thickness. [8]

1.5 Super exchange and double exchange

As mentioned before, the magnetic properties of manganites are influenced by exchange interactions between the Mn ion electron spins, which are controlled by the overlap between Mn d-orbitals and O p-orbitals. These are called superexchange interactions, depend on the orbital configuration and follow the rules of Goodenough-Kanamori [10], that state that the interactions are antiferromagnetic if the virtual electron transfer is between overlapping orbitals that are half-filled, or ferromagnetic in case the initial orbital is half or completely filled and the final orbital is empty or half filled, respectively.

In case the manganese ion changes to a higher valence, Mn^{3+} - O - Mn^{4+}, Mn can change their valence with a simultaneous jump of the e_g electron of Mn^{3+} to the O p-orbital and from here to the empty e_g orbital of Mn^{4+} [6]. A hole appears in the place where the electron was. Other e_g electron located at a neighbouring Mn^{3+} ion jumps to the new vacant place at the initial manganese trivalent ion [7]. This mechanism operating in mixed-valent manganites is called double-exchange (DE) and ensures a strong ferromagnetic interaction mediated by hopping electrons [6].

1.6 Colossal Magnetoresistance

Magnetoresistance (MR) is a property of materials that represents the change of electric resistivity caused by the application of a magnetic field [2] and is defined by equation (2). R(O) and R(H) represent the values of resistance in the presence and absence of a magnetic field, respectively.

$$\%MR = \frac{R(0) - R(H)}{R(O)} \times 100\% \quad \text{eq. (2)}$$

This definition leads to positive values for the CMR effects since R(H)<R(0).

While most ferromagnetic metals and alloys exhibit a MR only a few percent (until saturation), the resistivity value was noticed to change by several orders of magnitude in perovskite oxides in 1993 [11]. Since then, the phenomenon has been studied in extensive detail. The interest in this field arises due to the potential applications in magnetic recording and sensors.

In perovskite structure manganites such as $La_{1-x}Ba_xMnO_3$ colossal magnetoresistance behavior is found to be largest around Curie temperature and is strongly dependent of A site ions (in this case Lanthanum) [4].

Jun Zhang *et al.* studied the temperature dependence of the magnetoresistance finding CMR effect at or above room temperature for $x = 0{,}2$. For this level of doping the peak is located at $T = 315\ K$ and the MR value is 25%. In addition to that result, this study was made for different doping levels and it is observed that with x increasing the MR peak temperature increases, but the MR peak value decreases [8]. Figure 5 presents the temperature dependence of magnetoresistance ratio for $LaBaMnO_3/SrTiO_3$ thin films and Table 2 shows magnetoresistance values for different authors, doping levels and thickness.

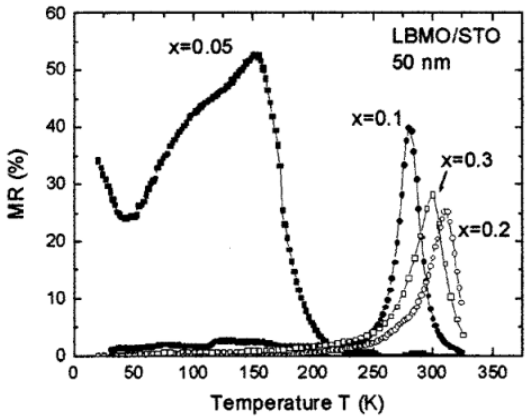

Figure 5 - Temperature dependence of magnetoresistance ratio for $LaBaMnO_3/SrTiO_3$ thin films. [8]

Author	Material	Substrate	Thickness (nm)	Field (T)	%MR
Jun Zhang *et al.*	$La_{0,8}Ba_{0,2}MnO_3$	$SrTiO_3$	50	0,8	2
Nagabhushana *et al.*	$La_{0.9}Ba_{0.1}MnO_{3+\delta}$	Bulk	-	1 7	5 62,5

Table 2 - Magnetoresistance values for different authors, doping levels and thickness [3], [8].

2 Magnetic Properties of Materials

2.1 Paramagnetism

When no external field is applied, paramagnetic materials present a random orientation of magnetic moments which cancel one another, setting the magnetization value to 0.

Differently, when a field is applied a tendency for each atomic moment to turn toward the direction of the field is noticed. With no opposing forces existing, a complete alignment of atomic moments is detected, forming a very large moment in the direction of the field. However, thermal agitation of the atoms opposes this tendency and tends to keep the atomic moments pointed at random, causing a small positive susceptibility (since only a partial alignment exists) [12].

An increasing temperature value causes an increasing randomizing effect of thermal agitation and therefore reduces the susceptibility [12].

In 1895 Pierre Curie published the first results on systematic measurements of susceptibility of a large number of materials at an extended range of temperature establishing that the magnetic susceptibility, χ_m, varied inversely with the absolute temperature, latter known as Curie law. *C* is the curie constant (related to the ionic/atomic magnetic moment)

$$\chi_m = {}^{C}/_{T} \quad (3)$$

If the magnetic ions in a solid exhibit some interaction, a more general law describes susceptibility.

$$\chi_m = {}^{C}/_{(T-\theta)} \quad (4)$$

θ is a called the paramagnetic Curie temperature, that increases for increasing ferromagnetic interactions. θ has temperature dimensions and is equal to zero for paramagnetic substances.

2.2 Ferromagnetism

First clarified by P. Weiss in 1907, ferromagnetism is a property that characterizes a strongly magnetic behavior. The origin of a strong magnetism are the magnetic interactions, which lead to the presence of a spontaneous magnetization caused by the parallel alignment of spins. The measured magnetization increases with the applied magnetic field.

When the external field is removed, the magnetism remains. This property of magnetic memory is named hysteresis. However, this behavior only happens below Curie temperature, T_C [12], [13].

Above the Curie temperature the material becomes paramagnetic (weak magnetic moment in the presence of the magnetic field) and Curie-Weiss law applies. That happens because above that temperature the thermal motion of the atoms is so violent that the electrons are no longer able to keep the spins aligned [12].

Table 3 presents Curie temperature and resistivity values for different authors, doping levels and thickness.

Author	Material	Substrate	Thickness (nm)	M(T)		Resistivity	
				Field (T)	T_C (K)	Field (T)	Transition T (K)
Daoudi *et al.*	$La_{0,7}Ba_{0,3}MnO_3$	$SrTiO_3$	60	-	300	-	-
			80	-	315	0,5	320
		$LaAlO_3$	60	-	280	-	-
			80	-	290	0,5	275
Nagabhushana *et al.*	$La_{0.9}Ba_{0.1}MnO_{3+\delta}$	Bulk	-	1	230	0	228
						1	230
Urushibara *et al.*	$La_{0,8}Ba_{0,2}MnO_3$	Bulk	-	-	-	5	310
Shulyatev *et al.*	$La_{0,85}Ba_{0,15}MnO_3$	Bulk	60	-	-	-	215
	$La_{0,8}Ba_{0,2}MnO_3$		80	-	-	-	330
Barnabé *et al.*	$La_{0,8}Ba_{0,2}MnO_3$	Bulk	-	-	258	-	-
Im *et al.*	$La_{0.7}Ba_{0.3}MnO_3$	Bulk	-	-	290	-	-
Urban *et al.*	$La_{0.7}Ba_{0.3}MnO_3$	Nanotubes	-	10	200	-	-
Zhang *et al.*	$La_{0,80}Ba_{0,20}MnO_3$	Bulk	-	0,02	280	-	< 50
	$La_{0,70}Ba_{0,30}MnO_3$				340	-	
	$La_{0,80}Ba_{0,20}MnO_3$	$SrTiO_3$	20	-	310	-	
	$La_{0,70}Ba_{0,30}MnO_3$				290	-	
	$La_{0,80}Ba_{0,20}MnO_3$		50	1	305	-	325
	$La_{0,70}Ba_{0,30}MnO_3$				295	-	310

Table 3 - Data collection related to Magnetization vs. Temperature and Resistivity values for different authors, doping levels and thickness [3], [4], [8], [14-18].

2.3 Antiferromagnetism

Antiferromagnetism is defined by neighboring spins being aligned antiparallel to one another so that their magnetic moments cancel.

When an external field is applied parallel to spin axis the spins that are parallel and antiparallel to the field experience almost no torque and so keep their ordered spin arrangement and only a small change of magnetization results.

As the temperature increases, the ordered spin structure tends to be destroyed and the magnetic susceptibility increases. However, it reaches a maximum point at critical temperature called Neél temperature , T_N. After that, the spin ordering starts disappearing [13].

3 Thin films

3.1 Growth process

The deposition of thin films involves four main sequential steps: I – vapor pulse, II – transport, III – growth, IV - analysis [19], [20].

I – vapor pulse

The source of film-forming material may be a solid, liquid, vapor or gas.

These processes can be separated in two main groups: physical vapor deposition (PVD), that involves solid materials, and chemical vapor deposition (CVD), that involves liquids, vapors or gases. The first group, PVD, used for this work, can be done by heat or by an energetic beam of electrons, photons (laser ablation) or positive ions (sputtering). [19].

II – transport

The major issue at this step is the uniformity of arrival rate over the substrate area [20]. Deposition behavior is determined by source and transport factors and by conditions at the deposition surface. The surface factors are the substrate surface condition (roughness, level of contamination, degree of chemical bonding with the arriving material and crystallographic parameters (in case of epitaxy)), reactivity of the arriving material (probability of arriving molecules reacting with the surface and becoming incorporated into the film) and energy input (can be associated to the substrate temperature, in the energy transported by ions when bombarding the substrate and also in the form of chemical energy due to the reactive source molecules and the molecules that have been dissociated in the course of vaporization or plasma transport) [19].

III – growth

The incident material loses the velocity component normal to the substrate (excepting when the incident energy is too high). When arriving to the substrate, material atoms or ions are physically absorbed on the surface and, since they initially are not in thermal equilibrium with the substrate, move over the surface. They interact with one another and form clusters.

The clusters are thermodynamically unstable and may tend to desorb after some time, depending on the deposition parameters. If the parameters are such that when another species collides with the cluster before this gets desorb they get absorbed, it starts to grow in size [20].

IV – analysis

This step is the final stage of process monitoring. Here one should observe the structure, composition and other properties of the film in order to see what the necessary changes are for a perfect gowth of the film in the next deposition.

3.2 Sputtering

First reported by Sir W. R. Grove in 1852 [20], sputtering is a high-energy vaporization technique in which the impinging atoms are accelerated to a range of energies that vary from a few eV to several keV. Virtually, any material can be vaporized and the condensation of this highly energetic vapour produces various growth features from polycrystalline layers to nanometer grain size, new crystalline phases, preferred orientation and epitaxy [21].

The sputter-deposition process may be divided into three subprocesses: I – decomposition of the target material, II – transmission of the vapor through the plasma and system gas to the substrate, III – condensation, nucleation and growth of the vapor material on a substrate [21].

As mentioned above, sputtering involves a collision of an incident particle with atoms within a few monolayers of a solid surface, the substrate. After the collision, the primary-recoil atoms collide with other atoms in the surface in a collision cascade. A surface atom is then ejected or sputtered if it receives sufficient energy to overcome its binding energy, which is approximately equal to its sublimation energy.

The sputtering rate is characterized by a sputtering yield, Y, which is the average number of emitted atoms per incident particle. The yield depends on the incident particle's energy and mass, the angle of incidence, the surface binding energy and the crystallinity of the target.

3.2.1 DC Sputtering – a general view of the technique

In this technique the material to be sputtered is set on the cathode and the substrate is fixed to the anode. Initially, the vacuum chamber is evacuated to about 10^{-4} Pa and filled with an inert gas to a pressure of 2 Pa. A negative voltage (range 1 – 5 kV) is applied to the target electrode and the substrate is held positive. The voltage is then increased until the gas particles are separated and a visible glow discharge appears above the cathode [21].

Positive ions from the plasma bombard the cathode and material from the target is sputtered and condenses on the substrate and chamber walls. Negative ions and electrons bombard the substrate surface [21].

The cathode dissipates heat due to ion impact while the anode becomes heated due to impacts making a water cool system needed.

However, this method cannot be applied to an insulator material because the glow discharge would not be sustained due to the immediate build-up of a surface charge of positive ions on the front side of the insulator. Nevertheless, this inconvenience can be managed using a RF power supply [20].

3.2.2 RF Sputtering

In this technique both the target and the substrate may be sputtered simultaneously, as initially observed by Robertson and Clapp in 1933 [20].

A high-frequency voltage is applied across the diode electrodes with sufficient amplitude to produce a glow discharge [21].

If the RF potencial is equally balanced between each electrode, both the target and the substrate are bombarded by positive ions and negative ions plus electrons during alternate half-cycles. Nevertheless, because the electron velocities are much higher than the ion velocities, a negative charge is accumulated on both electrodes. This phenomenon leads to the formation of negative steady-state DC potentials on the anode and the cathode relative to the plasma and ground potential [21].

3.2.3 Magnetron Sputtering

During the last decades, magnetron sputtering has become one of the leading techniques in the coating industry due to the fact that it allows for the versatile and precise control of the microstructure and related properties of the film such as its density, adhesion, surface roughness and crystallinity [22].

As Penning observed in 1935 while studying low pressure stuttering with a transverse magnetic field superposed on a dc glow discharge tube, the superimposed field lowered the sputtering gas pressure and increased the deposition rate [20].

The use of a magnetron incorporates a crosswise magnetic field over the cathode, trapping the beam electrons in helicoidal orbitals in that location therefore increasing their path length before their finally escape to the anode by collisional scattering. The efficiency of the process is then increased [19].

4 Characterization Techniques

4.1 X-Ray Radiation and Bragg's Law

X-Ray Diffraction (XRD) is a non destructive technique. It is sensitive to films thickness and provides information about the structure of the films or even about the different layers.

With the diffraction patterns it is possible to obtain information about, for example, the film thickness, the uniformity of epitaxial layers and the stress and strain in the sample [23].

X-rays are electromagnetic waves with wavelengths in the range between 0.1 and 10 Å. Since the lattice constants of crystals are of the same order of magnitude, x-rays are extremely useful in the analysis of crystal structure [23].

This type of radiation is produced when any electrically charged particle, usually electrons, of sufficient kinetic energy is rapidly decelerated. The radiation is produced in an x-ray tube that contains a source of electrons and two metal electrodes. The electrons are drawn to the anode due to the high voltage that is maintained across the electrodes. When the impact happens, x radiation is produced in all directions [24]. The rays coming from the target are a mixture of different wavelengths that depends on the tube voltage [24]. The radiation represented by such curves is called continuous, white or *bremsstrahlung*, which means 'breaking radiation', once it appears due to the electrons deceleration.

When the voltage on an x ray tube is raised above a certain critical value (characteristic of the target x-ray metal), sharp intensity maxima appear at certain wavelengths, superimposed on the rest of the spectrum [23]. The maxima are called characteristic lines and are very narrow. These lines may be defined as K, L, M, etc lines, as they increase in wavelength. Although, only the K lines are useful in x ray diffraction because the longer wavelengths are easily absorbed [23]. Though there are several lines in the K set, only the three strongest are normally observed: K_{α^1}, K_{α^2} and K_{β^1} [23].

Crystalline substances show characteristic patterns of reflected X radiation. One can observe that for defined incident directions peaks of scattered radiation (Bragg peaks) are observed.

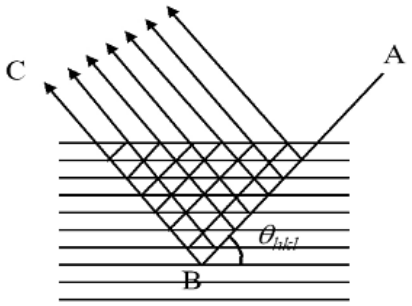

Figure 6 - Construtive interference of an x-ray and a crystalline structure. A) X-ray source, B) Atom located at a crystallographic plane, C) Constructive interference. [24]

$$n\lambda = 2d\sin\theta \quad (4)$$

The path difference between two rays is $2d\sin\theta$, where θ is the angle between the incident ray and the crystallographic plane. For interfering constructively, the path difference is an integral number of wavelengths. The integral number is the order of the Bragg reflection. The physical process is schematically shown in Figure 6.

4.1.1 θ/2θ scans – Bragg-Brentano geometry for films

θ/2θ scans serve to identify the crystallographic planes present in the crystal and are a direct consequence of the constructive interference explained in chapter 3.1.

The results obtained are a relation between a 2θ position and intensity. When compared to tabulated values, one can identify the plane families present in a crystal. To perform this measurement the

source is fixed while the detector and the sample move. The detector moves at twice the speed of the sample.

4.1.2 Crystallographic textures – Pole figures for films

Crystallographic textures studies serve to indentify orientations and structural defects and describe the orientations in 3D space of the individual cells. Textures are defined by the position of the unit cell in space and are represented in a stereographic projection [25].

Such a projection is obtained if one considers that the cell, located at the centre of the coordinate system, is surrounded by a unit sphere. The faces of the cell can be represented by tracing a vector perpendicular to them in the direction of the unit sphere (only directions to the northern hemisphere are considered). After connecting the points to the south pole, the intersection of these lines with the equatorial plane are called (face) poles and this is the image that are obtained when performing a crystallographic texture analysis.

To obtain a pole figure scans in three different sample axis should be preformed: ψ (between 0° and 90°), ϕ (between 0° and 360°) and θ. It is crucial that the axis are able to move independently from the source and the detector that, for this measurement, should be stable.

Axis 2θ, detector axis, and θ should be selected for a Bragg reflection and set stable while a simultaneous scan of axis ψ and ϕ is preformed.

Figure 7 presents the three types of scan preformed in order to obtain a texture. Figure 8 shows the crystal movements necessary to obtain a texture.

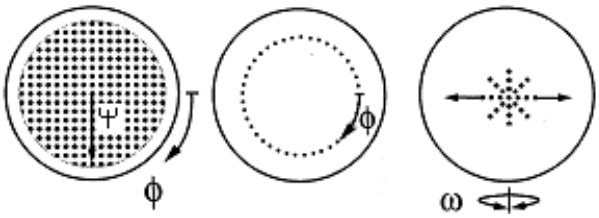

Figure 7 - Three types of scan preformed in order to obtain a texture. Adapted from [25].

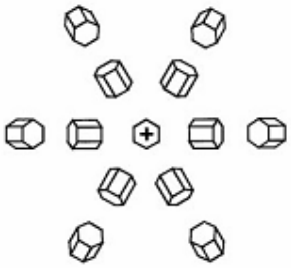

Figure 8 - Crystal movements related to textures. Plane initially considered (00.1). Adapted from [25].

4.1.3 High-Resolution Maps

Reciprocal space maps are a collected series of omega/2theta scans around a Bragg peak. Maps should be treated as rocking curves and allow the user to observe the crystallographic quality of the thin films.

Although one can notice the XRD pattern diagonally, individual 2θ scans for a range omega values can show the wideness of the peaks as well the presence of unexpected ones.

Additionally, when in reciprocal coordinates scale maps can grant information about the alignment of the film (target material) with the substrate.

4.2 Magnetization Measurements

4.2.1 Vibrating Sample Magnetometer (VSM)

First developed by Simon Foner in 1959 [26], the vibrating sample magnetometer measures the electromotive force (emf) induced by a magnetic sample when it is vibrating at a certain frequency and under the presence of a static and uniform field.

The measurements are based on the change of magnetic field flux in a sensing coil when a magnetized sample is vibrating near it. The sample is attached to a nonmagnetic support and then fixed to a mechanical vibrator. The sample movement creates an oscillating magnetic field that induces an alternating emf in the detection coils. The magnitude of the electromotive force is proportional to the magnetic moment of the sample. This emf is amplified with a lock-in amplifier that, after provided with a reference signal, is sensitive only to signals at the vibration frequency reducing the interference of other alternative voltages [12], [26].

The detection-coil arrangement shown is only one of several possibilities described by S. Foner [26]. Still, all the arrangements involve balanced pairs of coils that cancel signals due to variation in the applied field, spurious vibrations and electric signals [26], [12], [19]. The system should be calibrated with a specimen of a known magnetic moment that must have the same size and shape of the sample to be measured [12]. Figure 9 presents a schematic of a VSM.

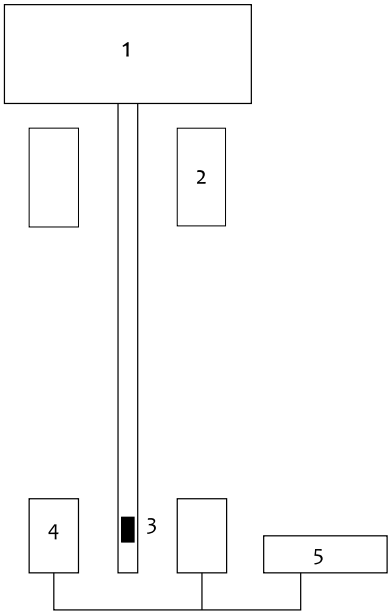

Figure 9 - Schematic of a vibrating sample magnetometer. Legend: 1) mechanical vibrator, 2) reference coil, 3) sample, 4) detection pairs, 5) lock-in amplifier and detection system.

4.3 Electric Measurements

4.3.1 Four-point probe technique

The four-point probe technique is a common method for measuring electrical resistivity and was originally developed by Wenner in 1915 and adapted for semiconductor resistivity by Valdes in 1954 [27].

The measurements are made with a four needle-like electrodes in a linear arrangement. A forced current *I* is injected through the outer pins 1 and 4, and the voltage drop is measured with pins 2 and 3 as represented in Figure 11. The measurements of the inner pin's voltage are made using a very high input impedance voltmeter in order to minimize the current flowing through them.

The purpose of using separate electrodes for the current injection and for the determination of the electric potential is to minimize the contribution of the contact resistance between the metal electrodes and the material.

The resistivity (ρ), current(I) and voltage(V) can be related by equation 5. A represents the cross section ($A = t \cdot w$) and L is the distance between the two inner electrodes, pin 2 and 3 [27].

For other conditions and geometries slightly different equations, differing by numerical factors, are used to obtain the materials resistivity.

$$\rho = \frac{V \cdot A}{I \cdot L} \quad (5)$$

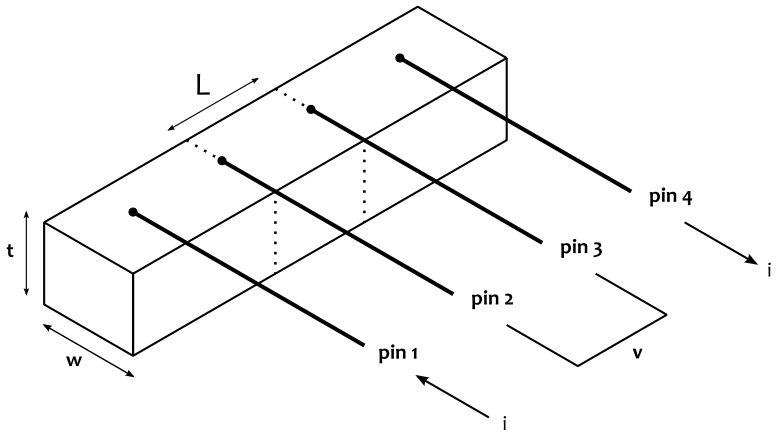

Figure 10 - Four-point probe technique schematics.

5 Experimental Procedure

5.1 Target

The sputtering target used has the composition $La_{1-x}Ba_xMnO_3$ (Kurt J. Lesker Company). According to the supplier the level of doping is $x = 0{,}30$ (XRD pattern of the target shown in Figure 11). However, XRD pattern peaks of all the thin films seem to be indexed according to data-sheets with a doping level of $x = 0{,}20$. The probable cause for this to happen is the fact that Barium atoms are heavier that Lanthanum and therefore harder to eject from the target and reach the substrates. XRD pattern for the target is shown in Figure 12 and peak indexation is established in Table 4.

The sputtering apparatus used has a vacuum system composed of 2 pumps. The first pump to be used is a rotary pump and the vacuum level obtained is 10^{-2} mbar. After that, the turbomolecular pump is used and a pressure of $5x10^{-8}$ is obtained. The chamber heats and Argon flows to the chamber (that should be at the same temperature used for the deposition). At this point, the chamber has a pressure of $5x10^{-3}$ mbar. The electric field is applied and the plasma is formed. Figure 13 exhibits the sputtering apparatus.

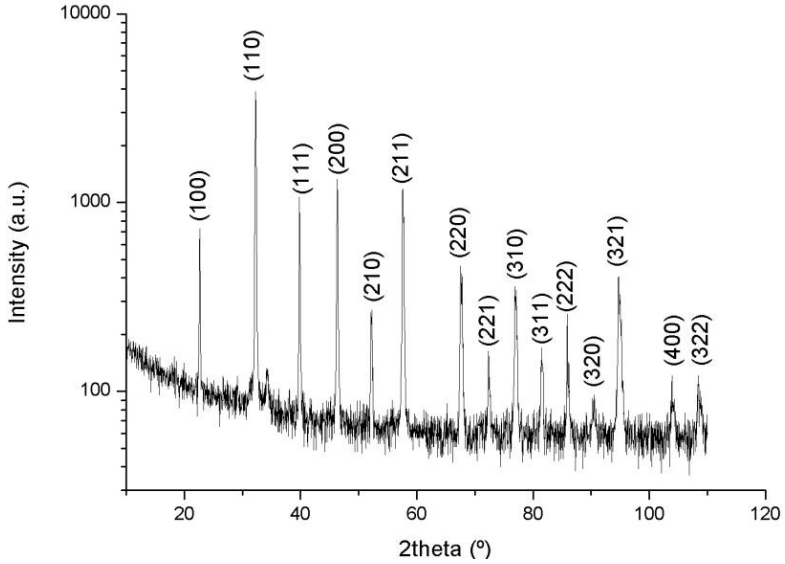

Figure 11 - XRD pattern for the used target $La_{0.7}Ba_{0.3}MnO_3$.

Peak position	Indexation
22,6583	(100)
32,2584	(110)
39,8015	(111)
46,3241	(200)
52,0885	(210)
57,5368	(211)
67,4735	(220)
72,2841	(221)
76,9084	(310)
81,3548	(311)
85,8188	(222)
90,5115	(320)
94,6059	(321)
103,7114	(400)
108,3029	(322)

Table 4 - Peak indexation for the used target – the values agree with cubic system.

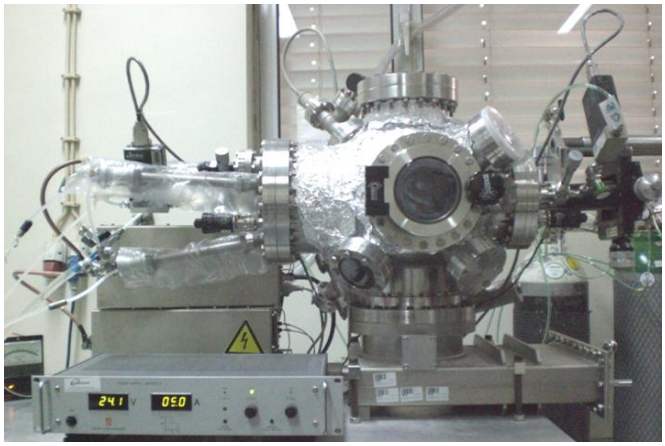

Figure 12 - Sputtering apparatus.

5.2 Substrates

Thin films were grown on sapphire (Al_2O_3) and MgO substrates kept at 757°. Sputtering parameters are similar however partial Argon during deposition and Oxygen after deposition pressures differ, in the sample batches prepared. Three sample batches were used, being the main difference the deposition time – Table 5. All substrates have an area of 10x10 mm^2 and a thickness of 0,5 mm.

The Al_2O_3 substrate series is composed by 3 thin films with different thickness.

The MgO substrate series is composed by 3 thin films also with different thickness.

	LBM 4	LBM 5	LBM 6
Time Pre-Sputter (min)	12	15	17
Deposition Time (min)	120	17	135
Argon Partial Pressure (mbar)	5 E -3	5,0 E -3	5,0 E -3
Oxygen Partial Pressure (mbar)	5,0 E -4	1,0 E -3	1,0 E -3
Heater Temperature (ºC)	757	757	757

Table 5 - Information regarding sputtering deposition for different series of thin films.

5.2.1 Al_2O_3

Al_2O_3 belongs to the space group R-3c (167). This material has an trigonal structure (equivalent to rhomboedrical) with parameters $a = b = c = 5{,}127$Å. Standard orientation of c-plane is $(0001) \pm 0{,}3°$. Table 6 gives the atoms positions for a sapphire cell.

	x	y	Z
Al	0,3551	0,3551	0,3551
O	0,5533	-0,5533	1/4

Table 6 - Atoms position for Al_2O_3 cell.

5.2.2 MgO

MgO has an cubic structure with parameters $a = 4{,}212$ Å. Table 7 gives the atoms positions for a manganese oxide cell.

	x	y	Z
MgO	0.0	0.0	0.0
O	0.5	0.5	0.5

Table 7 - Atoms position for MgO cell.

6 Structural Analysis - XRD

All the XRD data were obtained with a Phillips X'Pert MRD difractometer. The instrument has a 0,04rad Soller collimator that directs the beam to an anti-scatter slit ranging from $^{1}/_{8}^{\circ}$ to 2°. The beam is diffracted into the detector. The programmable slit may start at 1°. A Copper source is used to produce X-rays and has a characteristic wavelength of $\lambda = 1{,}5406$ Å. X-ray diffraction apparatus is shown in Figure 13.

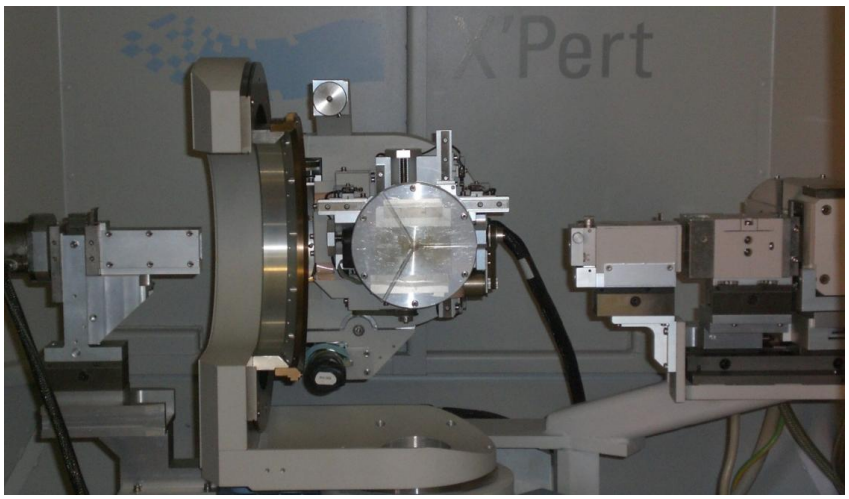

Figure 13 - X-Ray diffraction apparatus.

Film thickness was calculated based on the reflectometry data where a series of oscillations (kiessing firnges) are observed due to the interference of waves from both film surfaces. For that one has to upload the reflectometry data to Parratt © and simulate a fitting based on values of expected thickness, roughness and refraction index. The estimated error for this measurement is 15 Å. Figure 14, 15 and 16 represent the reflectometry data. Film thickness values from data analysis are present in Table 8.

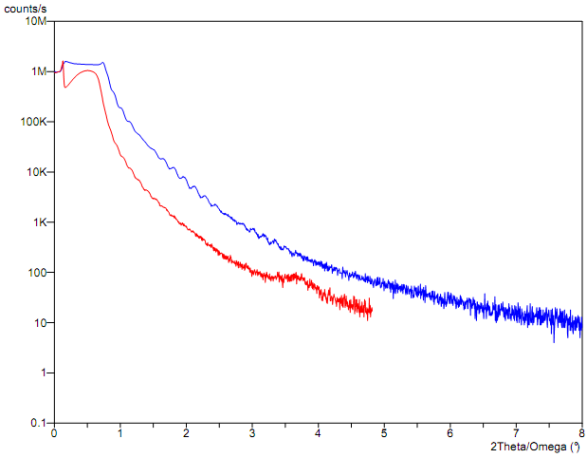

Figure 14 - Reflectometry for LBM4a and LBM4c.

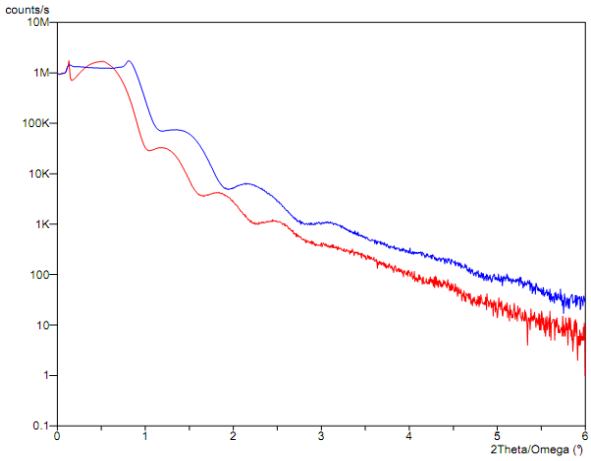

Figure 15 - Reflectometry for LBM5a and LBM5c.

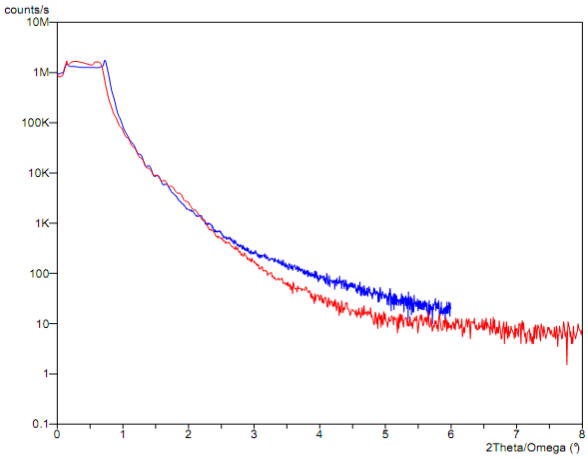

Figure 16 - Reflectometry for LBM6a and LBM6c.

Thin Film	Thickness (nm)
LBM4a	49
LBM4c	60
LBM5a	10
LBM5c	12
LBM6a	56
LBM6c	68

Table 8 – Film thicknesses.

6.1 θ/2θ scans

In several cases two peaks are observed instead of one. This happens because when the signal intensity is low the monocromathor is removed when performing the analysis.

It is important to clarify that all the plane families present in XRD pattern are parallel to the substrate surface although the quantity of cells with that orientation depends on the intensity of the peaks.

6.1.1 Al_2O_3 substrate

Though the substrate Al2O3 shows a trigonal structure, all the structural analysis was indexed based on the equivalent structure – rhomboedric. Figure 17 shows the XRD pattern for LBM4a, LBM5a and LBM6a and the peak indexations are presented in Table 9.

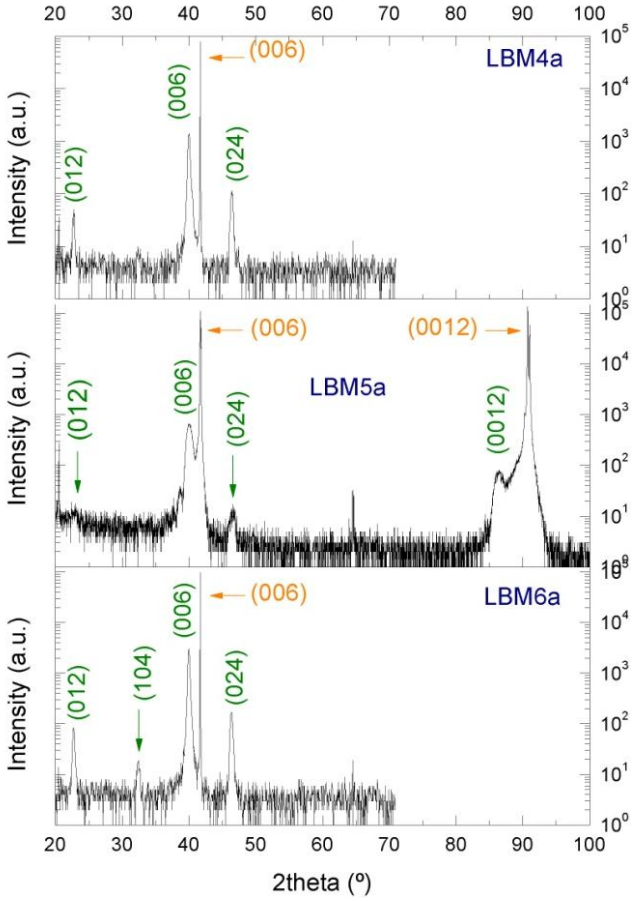

Figure 17 - XRD pattern for Al_2O_3 thin films. From the top: LBM4a, LBM5a, LBM6a. Orange: substrate peaks. Green: film peaks.

	LBM 4a	LBM 5a	LBM 6a
		Scan Parameters	
Start – End	20,025 ° - 70,975 °	20,010 ° - 104,990 °	20,025 ° - 70,975 °
Step	0,050 °	0,020 °	0,050 °
Thickness (nm)	49	10	56
		Film	
(01.2)	22,737 °	23,070 °	22,695 °
(10.4)	traces: 32,359 °	-	32,428 °
(00.6)	39,990 °	40,013 °	39,972 °
(02.4)	46,476 °	46,550 °	46,388 °
(00.12)	-	86,387 °	-
		Substrate	
Forbidden peak	20,528 °	-	-
(00.6)	41,679 °	41,743 °	41,688 °
(00.12)	-	90,789 °	-

Table 9 - Scan and peak parameters for Al_2O_3 substrate thin films.

For all the spectra it is observed that the substrate peaks are very narrow. Also, for all the thin films two families of planes are present: {00.1} and {01.2}, whereas in LBM6a a third family is also present {10.4}.

The peak (00.12) is only possible to observe in the thin film LBM5a as a result of the wider scan parameters. Nevertheless, this peak is expectable to be observed in the other thin films of this series.

The family of planes {00.6} appears both in the thin film and substrate leading to the conclusion that the film is well *c* oriented, in comparison to the other possible orientations. This illation is confirmed by the peaks relative intensity in Fig. 18, that exhibits the highest intensity for (00.6) plane.

Satellite peaks are observed for LBM5a on the left to the peak (00.6) and appear when the analyzed sample has a very low roughness.

A very weak peak belonging to the substrate is observed at LBM4a and LBM5a for $2\theta = 22°$ and consequently not indexed since it is not present in the XRD data-sheets consulted.

Although the most intense peaks belong to the thin film LBM4a and the least intense to LBM5a the relative intensities are constant for the different peaks. In addition, relative intensities presented in Figure 18 show that peak (10.4) should only be considered as a trace plane in all the films.

Out of plane lattice parameters of the rhomboedric film cell can be calculated from Bragg's equation for the interplanar spacing.

$$c = \frac{l \cdot \lambda_{Cu}}{2 \cdot \sin \theta_{h,k,l}} \quad (6)$$

Considering $l = 6$, $\lambda_{Cu} = 1{,}541$ Å and $\theta_{h,k,l} = 19{,}991°$, $c = 13{,}514$ Å.

Similarly, considering the distance between planes $d_{(024)} = 2{,}122$ Å and trigonometric relations, a mean value of *a* and *b* can be calculated and is 5,5473 Å.

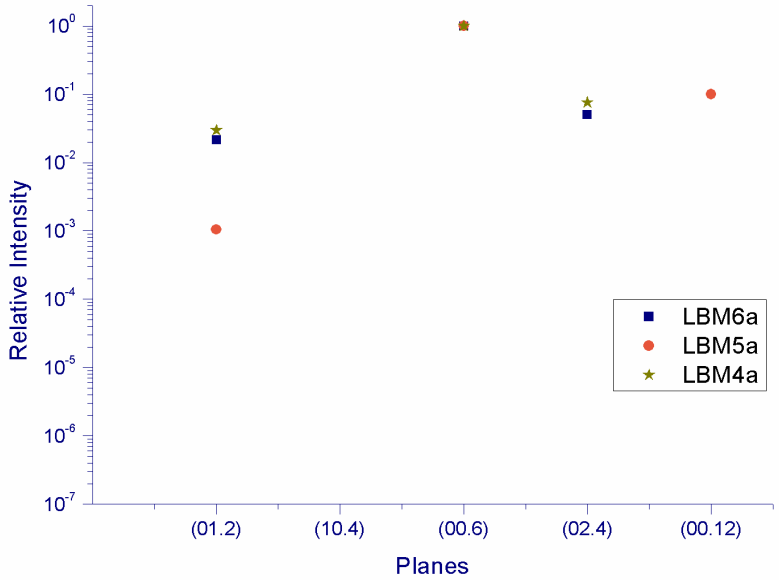

Figure 18 - Relative intensities of the observed peaks associated with different planes in the Al_2O_3 substrate thin films.

6.1.2 MgO substrate

Figure 19 shows the XRD pattern for LBM4c, LBM5c and LBM6c and the peak indexations are presented in Table 10.

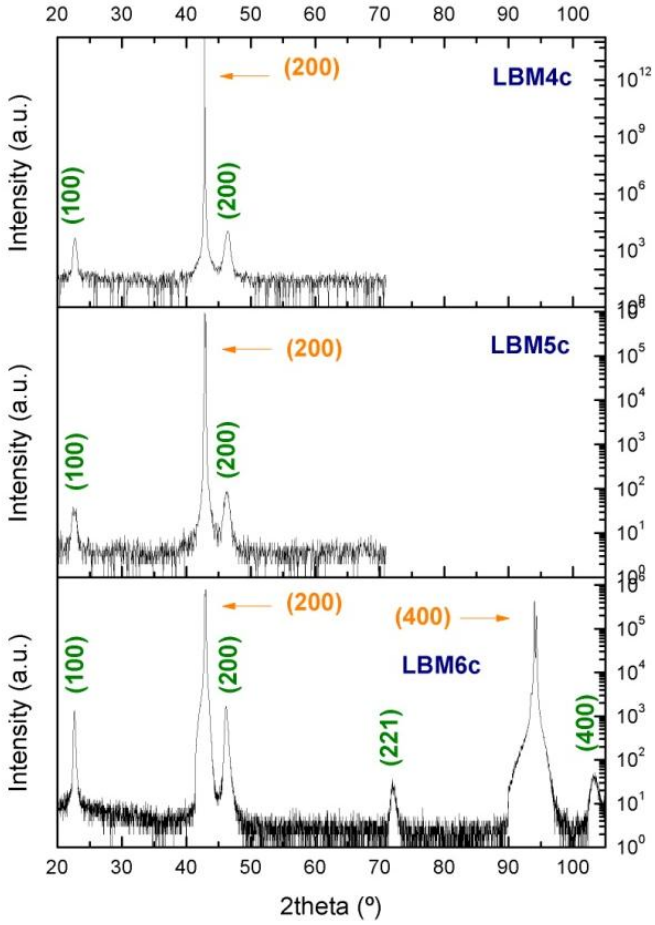

Figure 19 - LBM XRD pattern. From the top: LBM4c, LBM5c, LBM6c. Orange: substrate peaks. Green: film peaks.

	LBM 4c	LBM 5c	LBM 6c
		Scan Parameters	
Start - End	20,025 ° - 70,975 °	20,025 ° - 70,975 °	20,010 ° - 104,990 °
Step	0,050 °	0,050 °	0,020 °
Thickness (nm)	60	12	68
		Film	
(100)	22,694 °	22,652 °	22,585 °
(200)	46,454 °	46,399 °	46,130 °
(221)	-	-	71,978 °
(400)	-	-	103,376 °
		Substrate	
(200)	42,855 °	42,847 °	42,975 °
(400)	-	-	94,039 °

Table 10 - Scan and peak parameters for MgO substrate thin films.

In the all spectra only one family of planes is observed both for the substrate and the film: {100}. This allows the conclusion the film has adopted the substrate structure (information confirmed in chapter 5.2).

The cell parameters for these films can also be calculated similarly to the method used for Al_2O_3 cells, giving a mean value for *a*, *b* and *c* $a = 3{,}906$ Å.

6.2 Pole Figures

For the following results it is relevant to understand that a higher intensity results from a greater number of crystals oriented in that direction and, as a result, a lower intensity is related to a lower number of crystals with that orientation.

6.2.1 Al_2O_3 substrate

To understand the results is important to see how the substrate and the target material relate. The unit cells are represented in Figure 20 (xy projection).

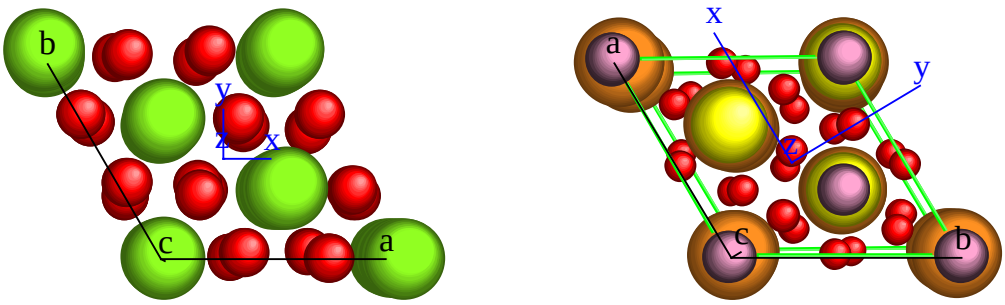

Figure 20 - On the left: Al_2O_3 cell (red: O, green: Al). On the right: rhomboedral LBM cell (yellow: La, orange: Ba, purple: Mn, red: O).

The distance between Al atoms is $5{,}13$ Å whereas the distance between atoms *a* and *c* in the LBM cell is $5{,}47$ Å. Due to the lattice mismatch, the relation of epitaxy is obtained with a compressive strain on the first layer of the film. As the film grows it relaxes to the values of the bulk material.

Table 11 presents the angle used to obtain the pole figures.

Plane	Angle		
	LBM 4a	LBM 5a	LBM 6a
(02.4)	46,380 °	46.650 °	46.380 °
(00.6)	40,030 °	40.048 °	39.780 °

Table 11 - Angle of pole figures – Al_2O_3 substrate thin films.

Using CaRIne Crystallography one can calculate the angle between planes, shown in table 12.

Plane 1	Plane 2	Angle between planes
(10.4)	(00.6)	35 °
(02.4)	(00.6)	70 °
(02.4)	(10.4)	54 °

Table 12 - Angle between planes – rhomboedric cell. Obtained with CaRIne Crystallography 3.1.

The results of pole figures are shown in Figure 21 (for substrate) and in the figures of Table 13.

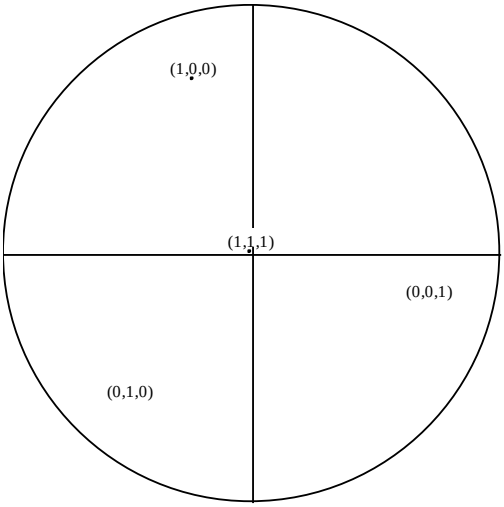

Figure 21 - Stereographic projection for a trigonal Al_2O_3 cell. The family of planes {100} is found at Ψ=71°. Indexation for a trigonal cell. Obtained with CaRIne Crystallography 3.1.

	LBM4a	LBM5a	LBM6a
(02.4)	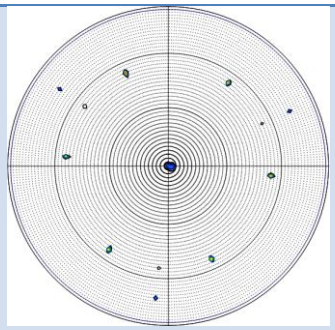 LBM(02.4) – ψ=0° LBM(00.6) – ψ=54,00° ? – ψ=54,00° Al_2O_3(100) – ψ=72,00°	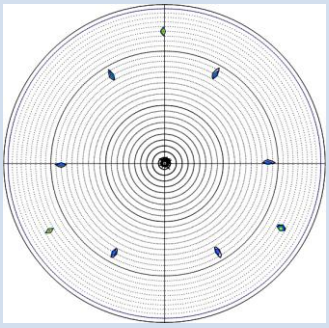 LBM(02.4) –ψ=0° LBM(00.6) – ψ=54,00° Al_2O_3(100) – ψ=72,00°	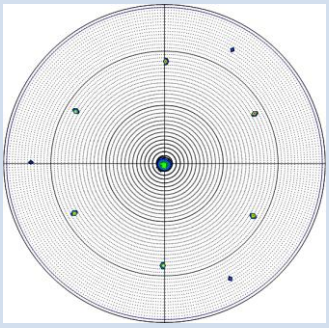 LBM(02.4) –ψ=0° LBM(00.6) –ψ=54,00° Al_2O_3(100) – ψ=72,05°
(00.6)	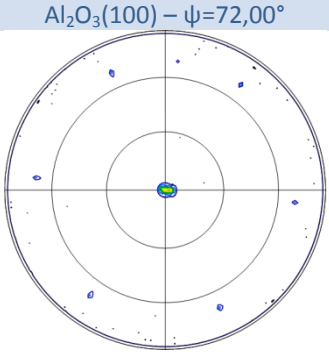 LBM(00.6) –ψ=0,00° LBM(10.1) – ψ=72,05°	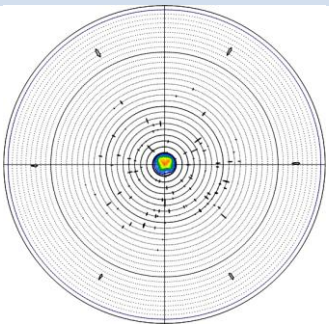 LBM(00.6) –ψ=0,00° LBM(10.1) – ψ=72,05°	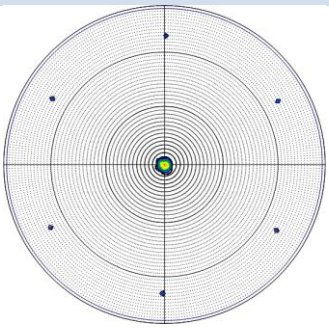 LBM(00.6) –ψ=0,00° LBM(10.1) – ψ=72,00°

Table 13 - Pole Figures for Al_2O_3 substrate thin films. Planes (02.4) and (00.6).

For both the textures (02.4) and (00.6) a central pole is distinguishable meaning that some crystal cells have this plane parallel to the substrate surface, as clarified in the XRD patterns analysis. That said, one can assume that crystals grew mainly *c* oriented but also with an angle of 70° from those cells (in order to reflect the plane (02.4)).

Textures (02.4) show the hexagonal parameters of the film cells. Poles at ψ=54,00° are not identified until now and require further investigation. Poles found at 72,00° are proved to belong to the substrate, Al_2O_3.

6.2.2 MgO substrate

Again, it is important to know how the substrate, MgO, and the target material relate. The unit cells are represented in Figure 22 (xy projection).

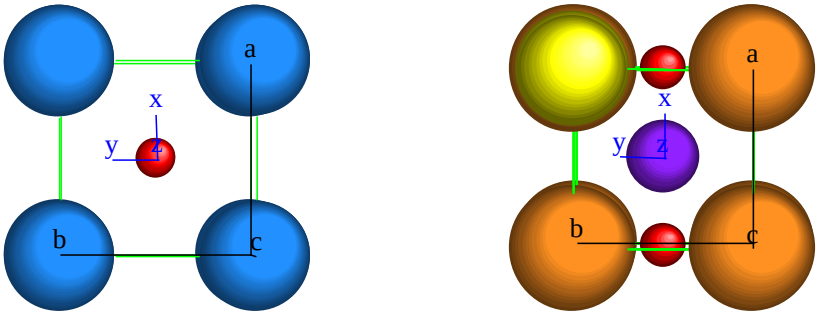

Figure 22 - On the left: MgO cell (blue: Mg, red: O). On the right – cubic LBM cell (orange: Ba, purple: Mg, yellow: La, red: O).

The cell parameters for MgO substrate are $a = 4{,}212$Å whereas in the LBM cell is $a = 3{,}906$ Å. The relation of epitaxy is accomplished because of the similar parameter values. Since the substrate is cubic and the target material has grown according to its structure, pole figures were performed to the planes (002), equivalent to (100), and (110) – since it is a cubic cell, it is not important whether the chosen plane is (110), (101) or (011) because the cubic organization will always be represented.

The angle of measurement of pole figures is present in Table 14 and Table 15 shows the angle between planes for a cubic cell. Table 16 shows the pole figure obtained for MgO substrate thin films.

Plane	Angle		
	LBM 4c	LBM 5c	LBM 6c
(110)	32,330 °	32,270 °	32,250 °

Table 14 - Angle of pole figures - MgO substrate thin films.

Plane 1	Plane 2	Angle between planes
(100)	(110)	45 °

Table 15 - Angle between planes – cubic cell. Obtained with CaRIne Crystallography 3.1.

	LBM4c	LBM5c	LBM6c
(110)	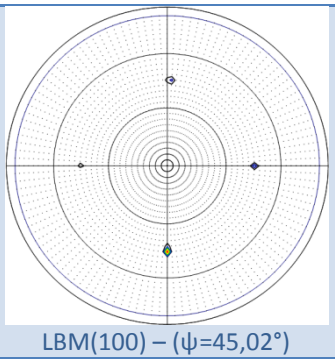	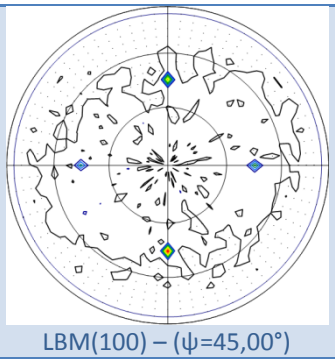	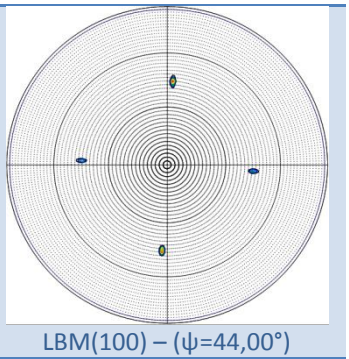
	LBM(100) – (ψ=45,02°)	LBM(100) – (ψ=45,00°)	LBM(100) – (ψ=44,00°)

Table 16 - Pole Figures for MgO substrate thin films. Planes (001), (002) and (110).

From the centered poles present in textures performed for the planes (001) and (002) it is possible to observe that the film grew perfectly oriented with the substrate material.

Also, textures (110) show four peaks and therefore confirm the cubic cells existing in the film. Poles at $\Psi \sim 45°$ are indexed as (100).

6.3 Reciprocal Space Maps

All the tables with peak indexation information are according to the XRD data shown in Chapter 6.1.

6.3.1 Al_2O_3 substrate

Table 17 presents the scan information regarding reciprocal space maps for LBM4a, LBM5a and LBM6a and Table 18 refers to the peak indexation on maps for Al_2O_3 substrate thin films. Figures 23, 24 and 25 show the maps on a logarithmic scale both for omega and 2theta coordinates and reciprocal space coordinates.

	2 theta		Omega		Step	Step-Time (s)
	Start	End	Start	End		
LBM 4a	31,05	48,95	14,00	26,00	2θ: 0,05 ω: 0,05	0,5
LBM 5a	31,04	48,96	14,00	26,00	2θ: 0,04 ω: 0,04	0,4
LBM 5a detail (10.4)	30,54	34,46	15,25	17,25	2θ: 0,04 ω: 0,04	3
LBM 6a	32,04	47,96	15,01	25,00	2θ: 0,04 ω: 0,03	0,5

Table 17 - Scan information regarding maps for Al_2O_3 substrate thin films.

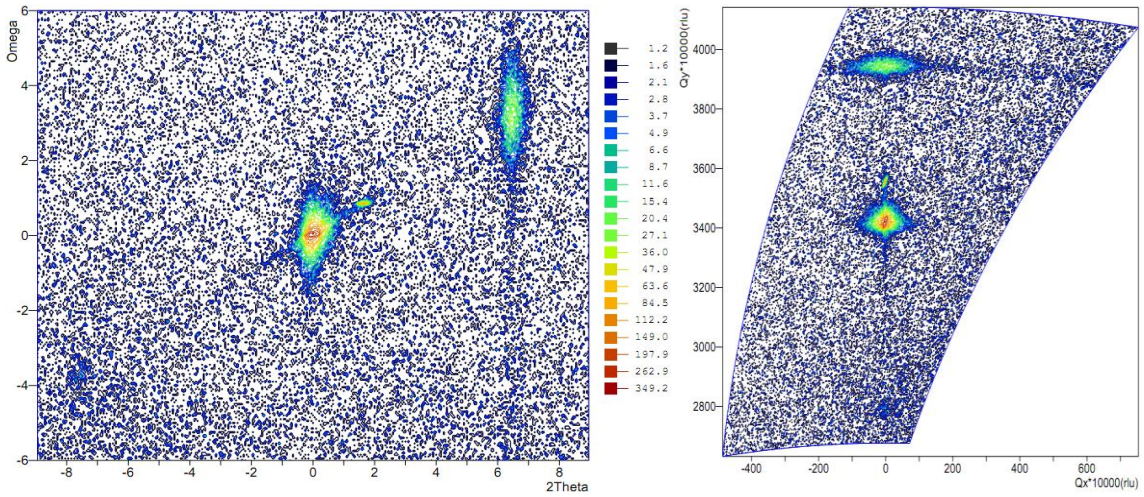

Figure 23 - LBM4a map. Logarithmic scale. On the left: omega and 2theta coordinates. On the right: reciprocal space coordinates.

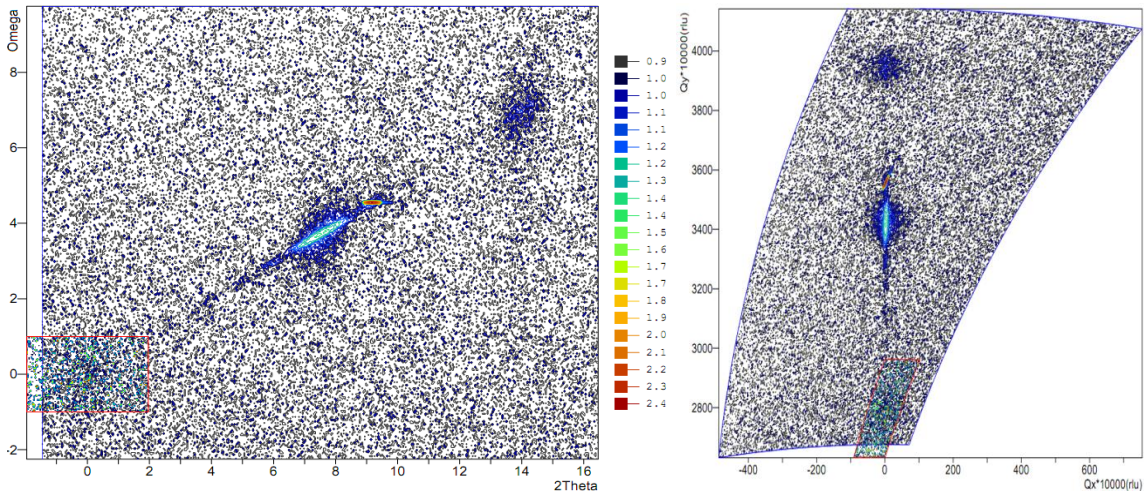

Figure 24 - LBM5a map. Logarithmic scale. On the left: omega and 2theta coordinates. On the right: reciprocal space coordinates.

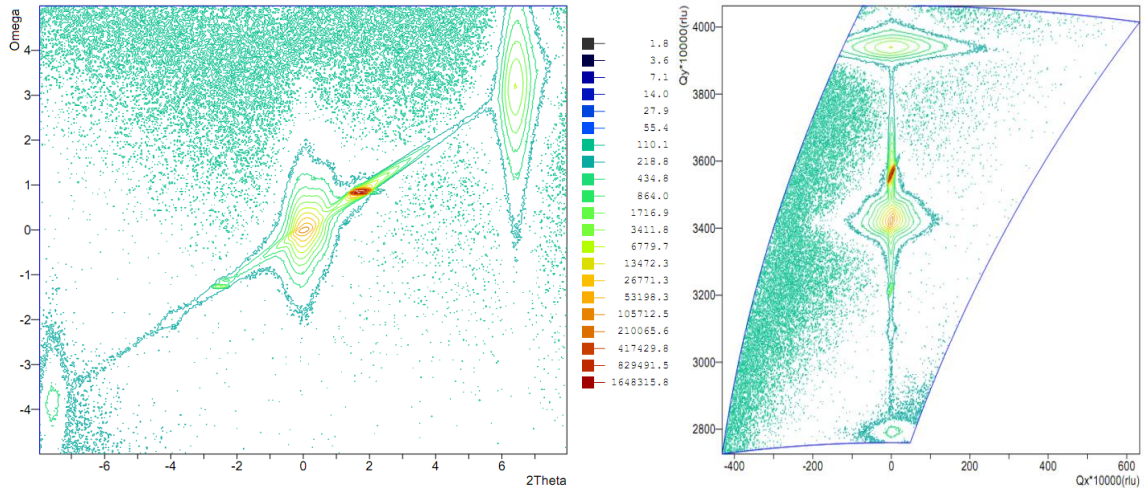

Figure 25 - LBM6a map. Logarithmic scale. On the left: omega and 2theta coordinates. On the right: reciprocal space coordinates.

Peak Indexation		LBM4a		LBM5a		LBM6a	
		Omega	2Theta	Omega	2Theta	Omega	2Theta
(10.4)	film	-	-	-	-	-	-
(01.2)	film	-	-	15,448	32,223	16,135	32,412
(00.6)	film	20,043	40,002	19,994	39,970	20,005	40,032
(00.6)	substrate	20,857	41,653	20,800	41,680	20,850	41,717
(02.4)	film	23,120	46,460	23,053	46,491	23,197	46,408

Table 18 – Peak indexation on reciprocal space maps for Al_2O_3 substrate thin films.

In all the maps four main peaks are observed. Three of them belong to the film and one is related to the substrate. It is important to keep in mind that the step values, step time and scale gradient differ from map to map and that leads to different resolutions and image quality.

Peak spread along omega is related to the crystallographic quality of the material. It is possible to observe in all the maps that the peaks FMWH grows larger with the film thickness. This situation is because a higher thickness value is proportional to higher tensions between atoms and consequently leads to a larger number of imperfections, associated with inhomogeneous strain.

It is possible to observe that the thin film with the smallest spread in omega is related LBM5a, the thinnest one and therefore that the peaks FMWH grows larger with the film thickness ($\Delta\omega_{LBM6a} > \Delta\omega_{LBM4a}$).

Contrary to θ/2θ information the high resolution detail around what was thought to be peak (10.4) proves that this peak is mainly background noise. The more defined area seen in LBM6a appears because of the high resolution used for that map as well as the lack of monocromathor.

Film peak (00.6) shows a higher intensity when compared with the substrate peak (00.6) both in LBM5a and LBM6a, as expected from the XRD pattern observed. However, this does not happen in LBM4a probably because of the higher step used here is not small enough to disclose the small centered area of the spot that should have the highest value. Moreover, the substrate peaks shape analysis show that the omega slits of the detector had a wider opening than the 2theta ones and the data-sheets from the substrate supplier mention a tilt of 3° of the planes. This might mean that if the map was focused on the film information, intensity variations of substrate peaks might be originated.

It is also important to mention that when observing the maps in the reciprocal space one can see that all the peaks are perfectly aligned and conclude that the growth process lead to a perfect orientation of the films when compared to the substrate.

All the results corroborate the XRD patterns obtained for this series.

6.3.2 MgO substrate

Table 19 presents the scan information regarding reciprocal space maps for LBM4a, LBM5a and LBM6a and Table 20 refers to the peak indexation on maps for MgO substrate thin films. Figures 26, 27 and 28 show the maps on a logarithmic scale both for omega and 2theta coordinates and reciprocal space coordinates.

	2 theta		Omega		Step	Step-Time (s)
	Start	End	Start	End		
LBM 4c	41,53	47,47	20,21	26,21	2θ: 0,03 ω: 0,04	1,0
LBM 5c	41,53	47,47	19,25	25,25	2θ: 0,03 ω: 0,03	1,0
LBM 6c	41,53	47,47	19,31	25,31	2θ: 0,03 ω: 0,04	1,0

Table 19 - Scan information regarding maps for MgO substrate thin films.

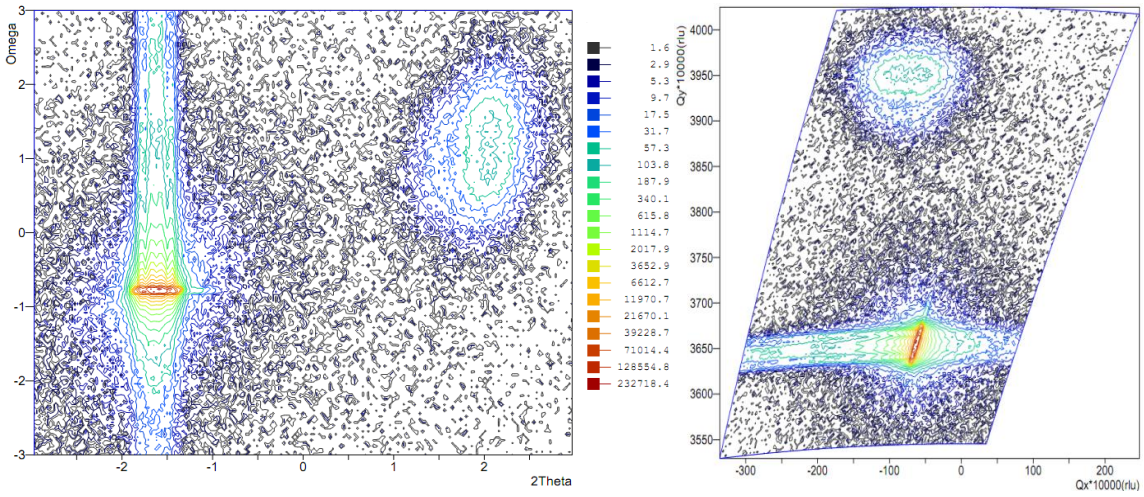

Figure 26 – LBM4c map. Logarithmic scale. On the left: omega and 2theta coordinates. On the right: reciprocal space coordinates.

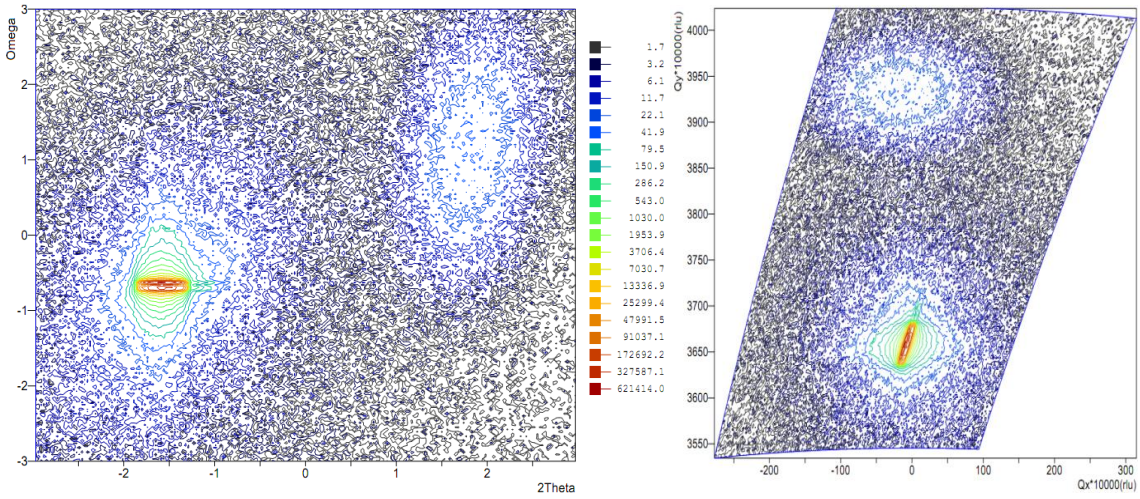

Figure 27 - LBM5c map. Logarithmic scale. On the left: omega and 2theta coordinates. On the right: reciprocal space coordinates.

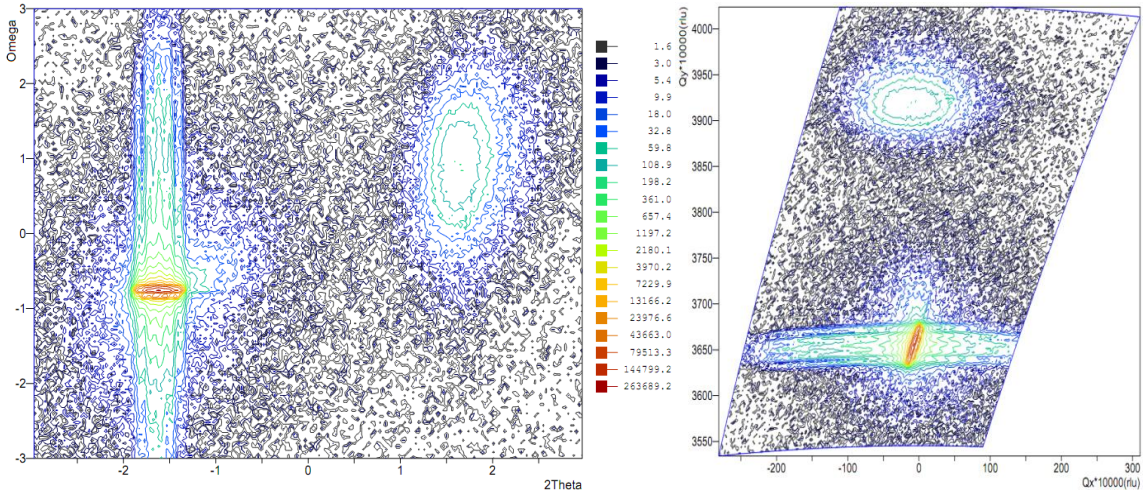

Figure 28 - LBM6c map. Logarithmic scale. On the left: omega and 2theta coordinates. On the right: reciprocal space coordinates.

Peak Indexation		LBM4c		LBM5c		LBM6c	
		Omega	2Theta	Omega	2Theta	Omega	2Theta
(200)	substrate	22,422	42,878	21,576	42,922	21,540	42,884
(200)	film	24,308	46,568	23,356	46,318	23,222	46,148

Table 20 - Scan information about reciprocal space maps for MgO substrate thin films.

All the maps show one peak from the substrate and another from the film, both indexed as (200).

First of all, it is necessary to establish that no changes are observed in the film peaks. Considering that all the thin films passed through the same procedure during growth, it is observed that the thinner film LBM5a has the smallest spread in omega for the substrate peak. For that reason the most probable conclusion is that this spread is related to interdiffusions in the interface between the substrate and the target material that alter the crystallographic quality of the substrate and give an inhomogeneous initial growth. In addition, the double peaks present in LBM5a are caused by the lack of use of a monocromathor.

As in the case of the previous series, the reciprocal space analysis of the maps exhibit a perfect alignment of both peaks and so a perfect orientation of the films with the substrate is confirmed.

7 Magnetic Measurements

The vibrating sample magnetometer instrument used in this work (from Cryogenics, UK) has a superconducting magnet which produces magnetic fields up to ± 10T. The VSM has a sensibility of 10^{-5} emu. It is possible to obtain magnetization vs. magnetic field data (M(H)) or magnetization vs. temperature (M(T)), in the range of 2 to 320K, and a closed-cycle cryogenic system is used to obtain lower temperatures. VSM apparatus is shown in Figure 29.

Figure 29 - VSM apparatus.

The apparatus used for resistance and magnetoresistance analysis (Four-point probe technique) is inserted in a dewar flask liquid nitrogen to lower the temperature. It has a temperature range from 77K to 400K which are read with a K type thermocouple. The temperature controller has a resolution of 0,01K and was bought from LakeShore Cryotronics, Inc., Model 325. The NanoVolt/Micro-Ohm Meter has a sensitivity of 100nΩ and the model is Agilent 34420A. NdFeB permanent magnets are used with a continuous magnetic field up to 1T intensity. The magnetic controller is a multimag magnet, from Magnetic Solutions. The vacuum pump used is a diaphragm vacuum pump able to reach 1,5 mbar (Vacuumbrand MD 1). The thermal contact between the sample and the nitrogen is provided with Helium. Four-point probe technique apparatus is shown in Figure 30.

Figure 30 - Four-point probe technique apparatus.

7.1 Magnetization as a function of the applied magnetic field and as a function of temperature

In the following it is presented the magnetic studies on the samples. Hysteresis cycles (M(H)) were measured at 3 temperatures 5, 150 and 300K typically up to ± 2 Tesla, enough to saturate the sample and determine the diamagnetic substrate contribution. The temperature dependence of the magnetization at applied field 0,2 T (enough to reach saturation) was measured between a low temperature (5 – 150K, below T_C) up to the maximum temperature available (300 – 320K).

Some measurements were also preformed in a SQUID magnetometer in the Physics Department of the Faculty of Science of Lisbon University, with Professor Margarida Cruz.

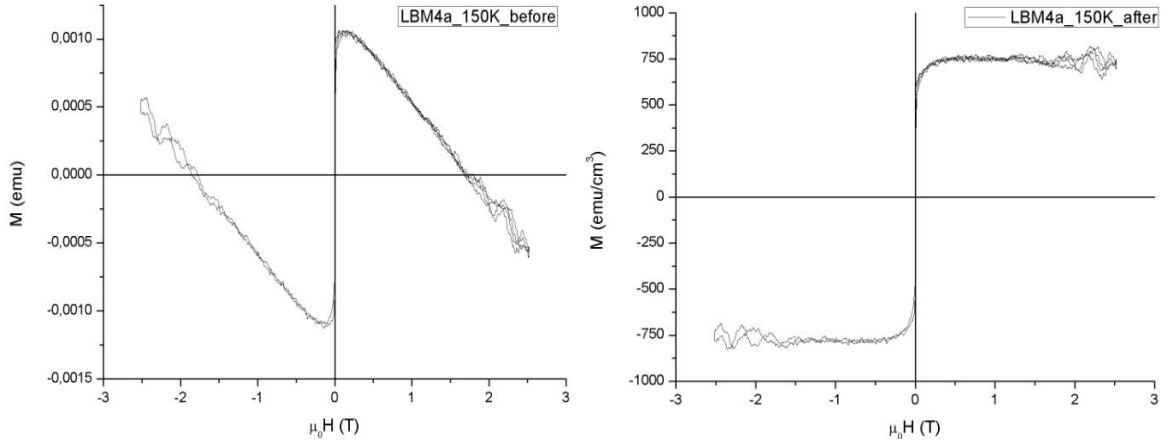

Figure 31 – Hysteresis loop for LBM4a at 150K. On the left: before removing the substrate contribution. On the right: after data treatment and without the substrate contribution.

The presence of the diamagnetic substrates give the measured magnetization curves a negative slope at high fields. In order to analyse the results the substrate contribution must be subtracted. For that, one has to consider that $M_{film} = M_{measured} - \chi_{diamagnet} \cdot H$, where $\chi_{diamagnet}$ is the high field slope after saturation. Since the samples have different film areas and thickness, it is important to obtain magnetization normalized values per cm^3. The area of the film is obtained with scanned images with a millimeter paper background. After, the M(H) hysteresis loop might still (in some cases) have to be corrected vertically, in order for it to be symmetric to $y = 0$. Figure 31 shows the hysteresis loop for one of the used samples before and after data treatment.

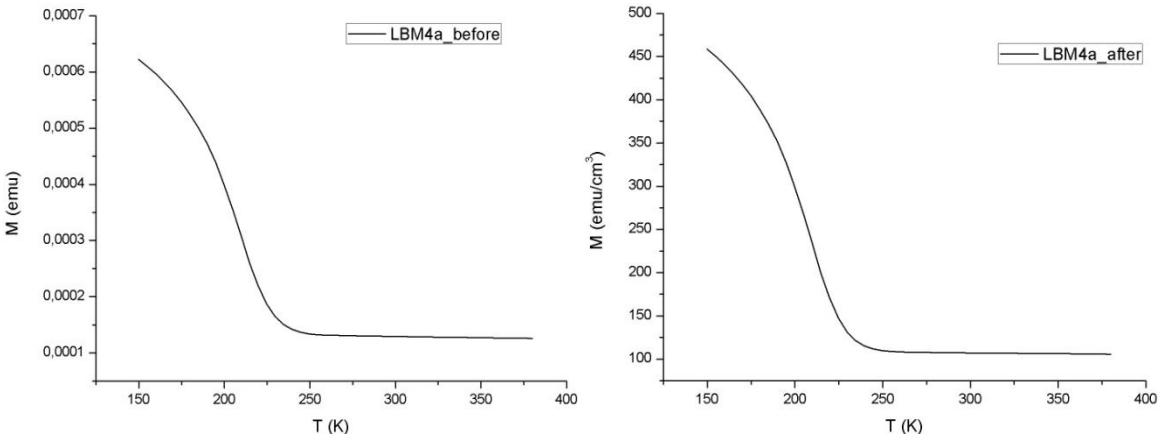

Figure 32 – M(T) for LBM4a. On the left: before removing the substrate contribution. On the right: after analysis and without the substrate contribution.

The case of magnetization measurements as a function of temperature is similar. Since the total magnetization combines the film magnetization and the substrate, $M_{total} = M_{film} + M_{substrate}$, the substrate contribution should be removed ($M_{substrate} = -|\chi| \cdot H$). For that, one has to multiply the M(H) slope for the field intensity at which it was measured and subtract the value to the data obtained. After that, is important to divide the obtained values for the film volume, as before. Figure 32 shows the magnetization as a function of temperature data for one of the used samples before and after data treatment.

Magnetization as a function of temperature measurements were obtained with a magnetic field of 0,2 T or 0,03 T (LBM4a, LBM5a and LBM5c).

It is important to keep in mind that the associated error for the absolute magnetization value [in emu/cm^3] is the sum of the partial errors: the area measurement error, the instrument of measuring the area error and the VSM error. However, one will consider that the VSM is about 8%, calculated based on the average proportion between the noise and difference between the positive and the negative magnetization.

7.1.1 Al_2O_3 substrate

Figure 33, 34 and 35 show magnetization as a function of field data for LBM4a, LBM5a and LBM6a, respectively, for a set of temperatures of 5K, 150K and 300K.

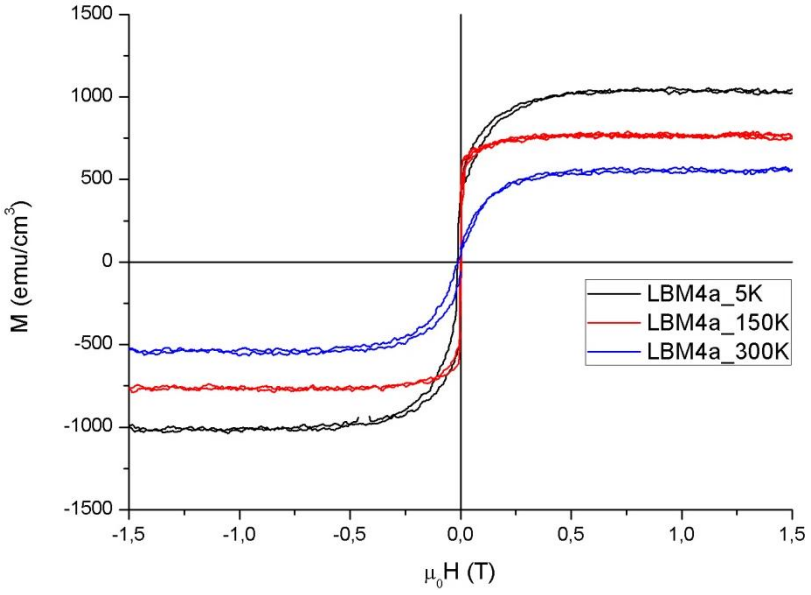

Figure 33 - M(H) for LBM4a. Temperatures of 5K, 150K and 300K.

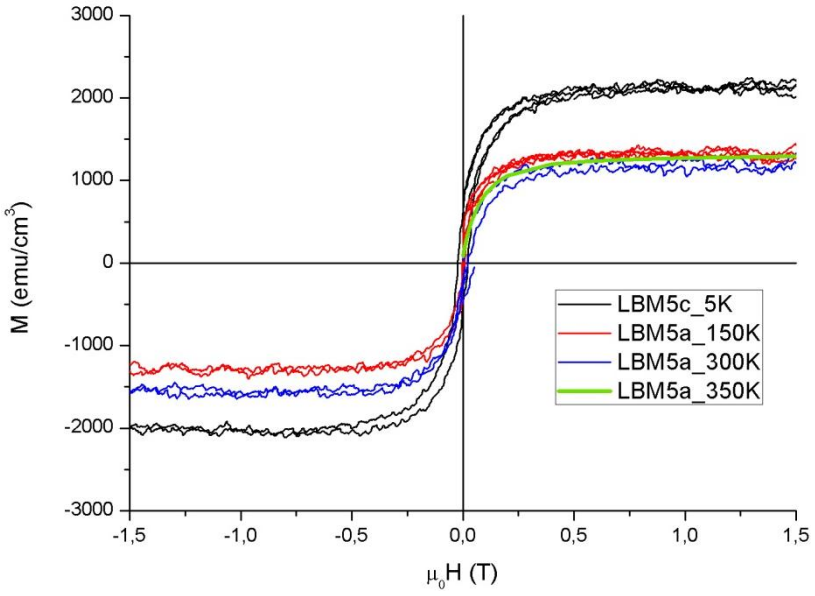

Figure 34 - M(H) for LBM5a. Temperatures of 5K, 150K and 300K.

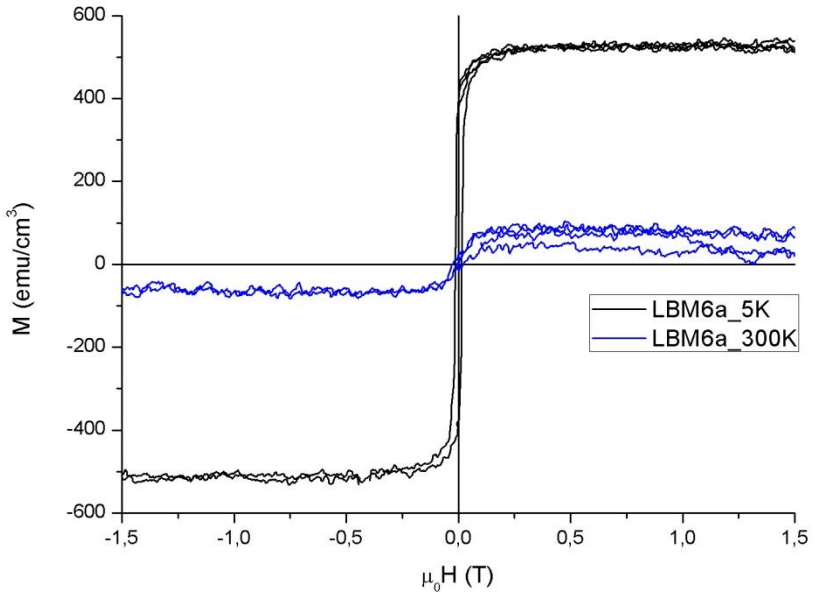

Figure 35 - M(H) for LBM6a. Temperatures of 5K and 300K.

Temperature dependence of the magnetization is presented in Figure 36, measured in magnetic field of 0,2 T for sample LBM6a (VSM) and 0,03 T for samples LBM4a an LBM5a (SQUID).

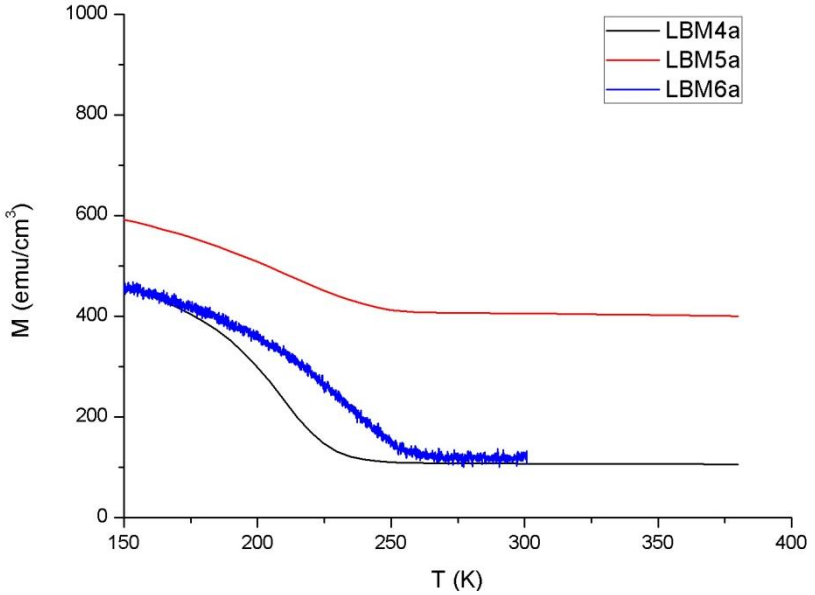

Figure 36 - M(T) for Al_2O_3 substrate thin films.

The temperature dependence allows to estimate the critical temperature TC, by the inflexion point (minimum of $^{dM}/_{dT}$). One can see that a substantial magnetization remains up to room temperatures or even higher (380K), well above known T_Cs for La-Ba manganites.

Table 20 summarizes the results of saturation magnetization and T_C for films.

	Thickness (nm)	Magnetization 5K (emu/cm^3)	Magnetization 150K (emu/cm^3)	Magnetization 300K (emu/cm^3)	M_{300K}/M_{5K}	T_C (K)
LBM4a	49,3	1100	770	560	53 %	209
LBM5a	10,0	2000	1300	1100 / 1200*	53 %	210
LBM6a	56,5	520	N/A	70	14 %	235

Table 21 - Magnetization values and Curie temperatures for Al_2O_3 substrate thin films. (*magnetization at 350K)

Comparing the magnetization values at RT and 5K is possible to conclude that LBM4a and LBM5a present a decrease to 55% while LBM6a only has around 14% at room temperature.

Magnetization values for all temperatures and films decrease with an increasing thickness.

Comparing to the existing saturation magnetization values in the literature for bulk manganites (single or polycristals) (500 emu/cm^3 at RT [1]), some of the obtained values in LBMa thin films (1000 emu/cm^3 at RT) are not expected since bulk materials have a minimum number of defects and do not present interface adjustments. Whether the obtained values are reasonable or not is something that requires further study.

Transition from ferromagnetic to the paramagnetic state is not fully observed because at room temperature (or higher temperatures) a magnetization value of zero is not obtained. One can notice that measurements M(T) still show a high magnetization at 380K for all LBMa. That is not expected since T_C is associated with a transition to a paramagnetic state and therefore a considerable reduction of the spins orientation (around zero). This remaining magnetization after the determined T_C can lead to the idea of a second Curie temperature associated with the remaining material existing at high temperatures. If so, that would mean that the thin film is not homogeneous.

7.1.2 MgO substrate

Figure 37, 38 and 39 show magnetization as a function of field data for thin films grown in MgO substrate for a set of temperatures of 5K, 150K and 300K. Magnetization as a function of temperature is presented in Figure 40.

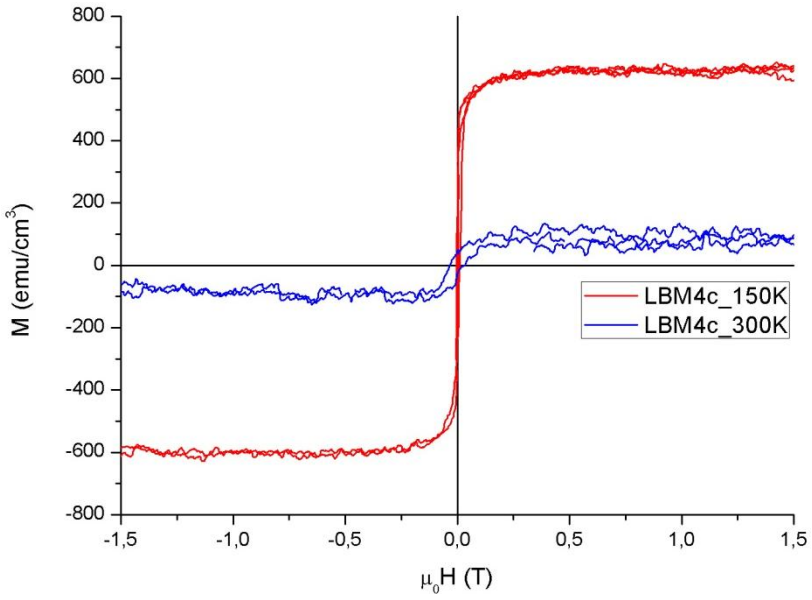

Figure 37 - M(H) for LBM4c. Temperatures of 150K and 300K.

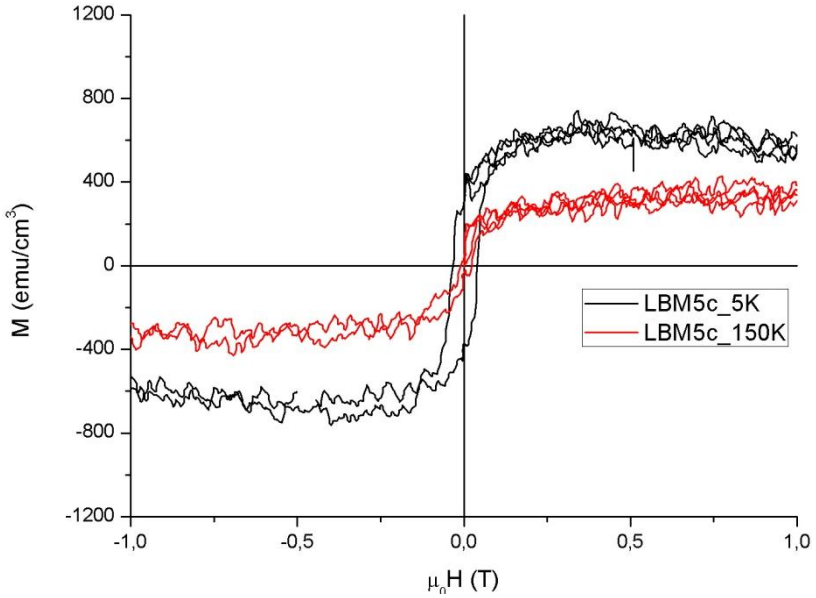

Figure 38 - M(H) for LBM5c. Temperatures of 5K and 150K.

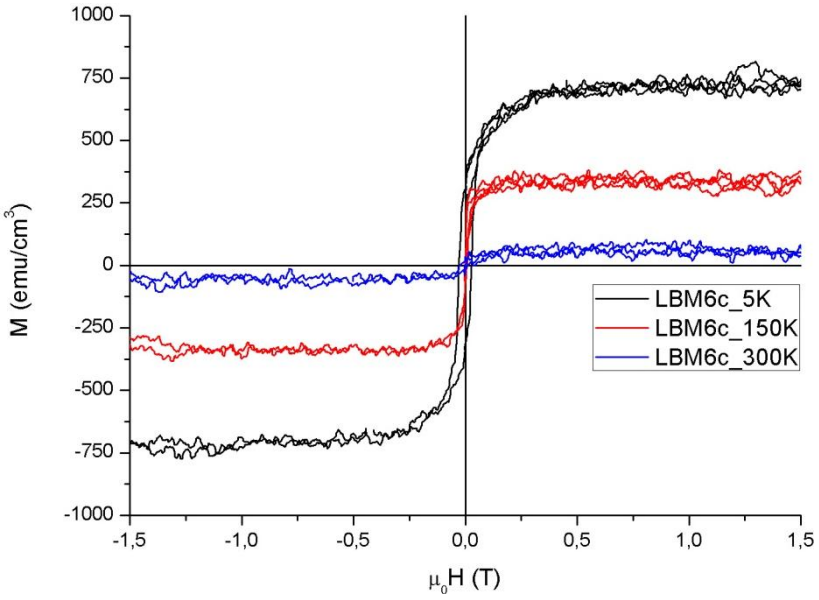

Figure 39 - M(H) for LBM6c. Temperatures of 5K, 150K and 300K.

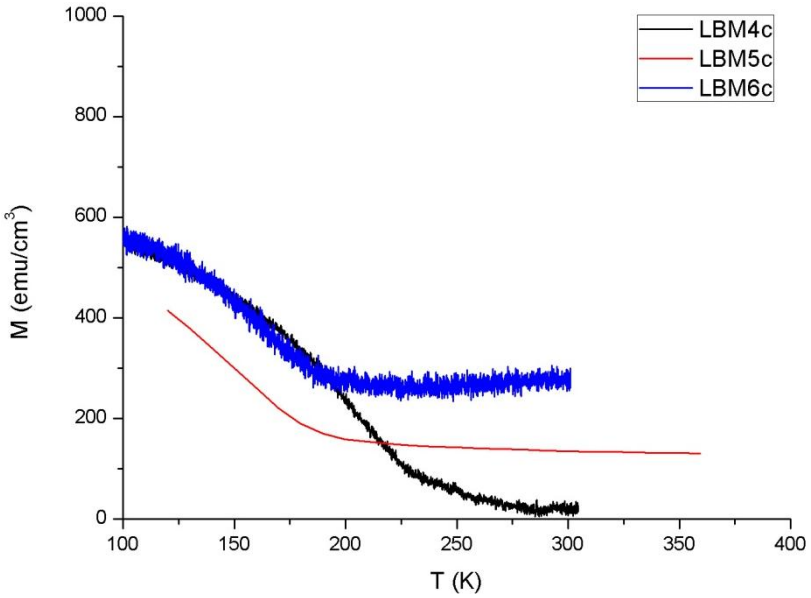

Figure 40 - M(T) for MgO substrate thin films.

	Thickness (nm)	Magnetization 5K (emu/cm^3)	Magnetization 150K (emu/cm^3)	Magnetization 300K (emu/cm^3)	M_{300K}/M_{5K}	T_C (K)
LBM4c	62,0	N/A	620	100	N/A	200
LBM5c	12,71	620	330	N/A	N/A	156
LBM6c	68,99	720	340	60	8 %	163

Table 22 - Magnetization values and Curie temperatures for MgO substrate thin films.

From the data presented it is easy to conclude that thin films grown in MgO have a very small amount of oriented spins at room temperature, in comparison to 5K. LBM5c is the thin sample that reflects that the most, since no magnetization signal is obtained at 300K meaning that at that temperature there is no orientation of spins left.

Magnetization curve for LBM5c at 300K is not shown because the value is so small that it should be considered as noise.

Curie temperatures arebetween 150K and 160K, although this is not observed for sample LBM4c. The reason for that is probably the difference in the oxygen partial pressure of the film growth. It is also important to mention that only for LBM4c the magnetization value decreases to 0 at room temperature. Is it possible that a second T_C will be found at higher temperatures for samples LBM5c and LBM6c.

7.2 Resistance and Magnetoresistance

Magnetoresistance values were obtained based on equation (2) from Chapter 1.6. The minimum value represents the point where there is a change in the conductive behavior of the sample and the corresponding temperature (critical temperature) should correspond to the Curie temperature, obtained in the M(T) data.

Measurements with 1T field intend to expose resistance change due to the orientation of spins when compared to the no-field situation.

The temperature dependence of the samples was measured in the interval 80K to 360K at magnetic field $H = 0$ and $\mu_0 H = 1T$. From the difference if the two curves the corresponding magnetoresistance values are obtain.

7.2.1 Al_2O_3 substrate

Figure 41 and Figure 42 show resistance and magnetoresistance dependence of temperature for LBM4a and LBM5a, respectively.

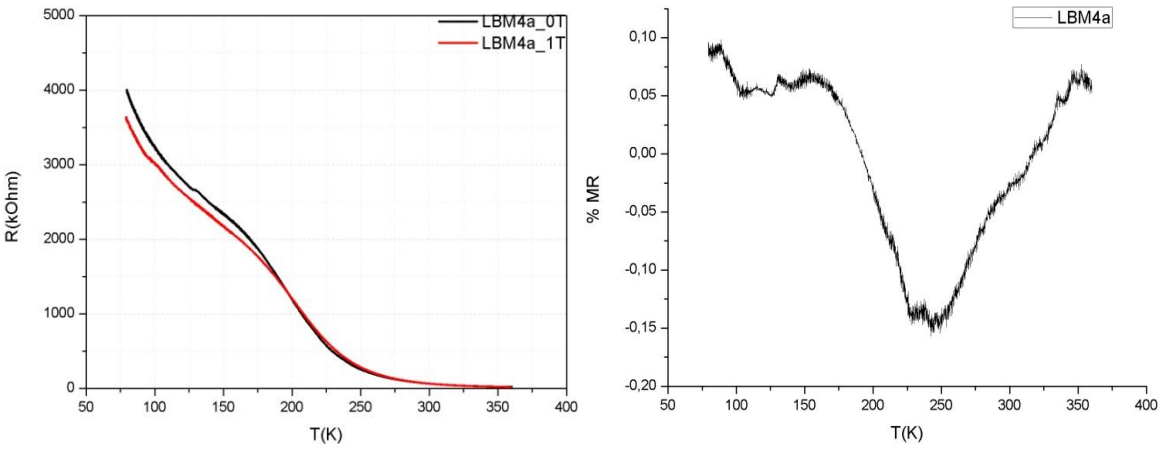

Figure 41 – LBM4a. On the left: R(T). On the right: MR(T).

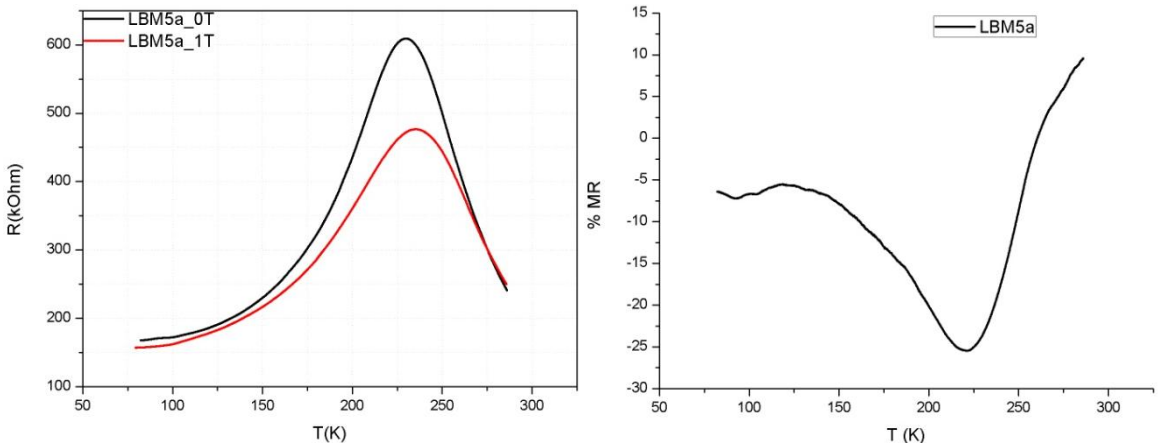

Figure 42 – LBM5a. On the left: R(T). On the right: MR(T).

	% MR	T_{MR}^{max}(K)	T_C (K)
LBM4a	17	240	209
LBM5a	25	220	210

Table 23 - Magnetoresistance and temperature values for samples LBM4a and LBM5a.

For both films the resistance and temperature values for samples LBM4a and LBM5a decreases with an increasing magnetic field. In the absence of magnetic field the manganese ions spins might not be parallel and the electron transfer is difficult, leading to higher values of resistance. When the magnetic field is applied the Mn ions spins are aligned and the transfer of electrons is easier, forcing lower values of resistance.

In LBM4a thin film one can see that though it shows a mainly insulator behavior, an inflexion point can be observed around 240K (information supported by MR(T) data). However, it is also clear that an insulator phase is superimposed in the metallic phase because the R(T) data shows a continuous decrease of resistance as the temperature gets higher.

LBM5a data show a different situation. It is absolutely clear from the resistance behavior that there is a metallic and insulators phase regions with a transition from metallic to insulator around 220K. This behavior is expected for manganites in this composition range.

Differences for the maximum magnetoresistance temperature and the Curie temperature might be due to the percolation regime of electrical conduction.

Unfortunately, the temperature at which the transition is observed limits possible applications of this material, since most applications envisaged are developed to operate at room temperature.

7.2.2 MgO substrate

Figure 43 and Figure 44 show resistance and magnetoresistance dependence of temperature for LBM4c and LBM5c, respectively.

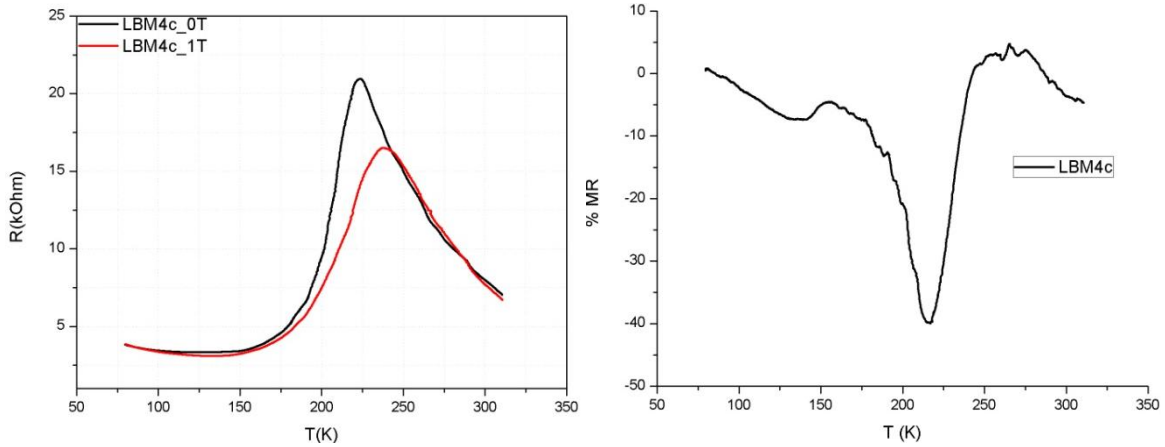

Figure 43 – LBM4c. On the left: R(T). On the right: MR(T).

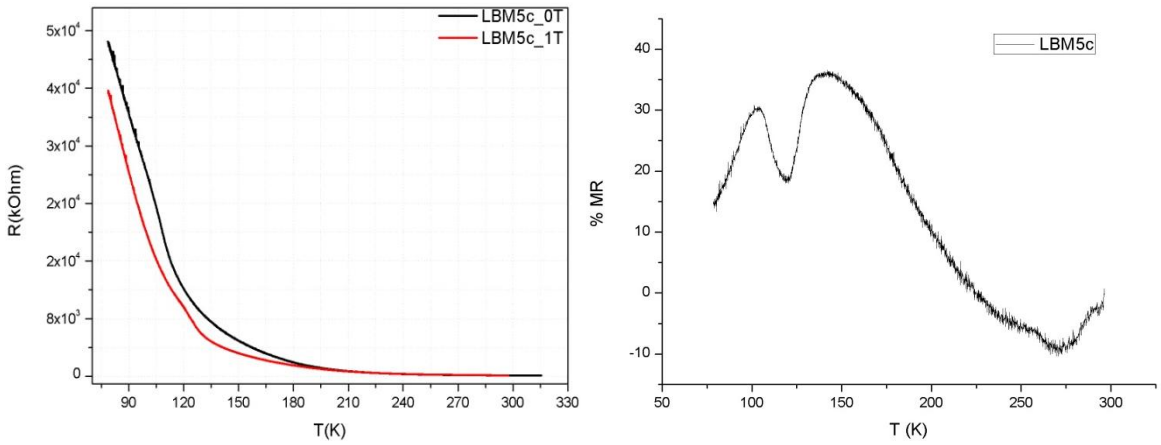

Figure 44 - LBM5c. On the left: R(T). On the right: MR(T).

	% MR	T_{MR}^{max}(K)	T_C (K)
LBM4c	40	216	200
LBM5c	36	140	156

Table 24 - Magnetoresistance and temperature values for samples LBM4c and LBM5c.

As in the thin films of Al_2O_3 substrate, resistance for LBM4c and LBM5c decreases with an increasing applied magnetic field.

LBM4c shows an transition from metallic to insulator phase around 216K and has a magnetoresistance of 40%.

LBM5c exposes a mainly insulator behavior of the sample with an inflexion point at 140K. Again, differences for T_{MR}^{max} and T_C might be due to the percolation regime.

8 Conclusion

The thin films grown in Al_2O_3 substrate have a rhomboedric crystalline symmetry and show three possible orientations, being the main one parallel to the substrate orientation. Therefore, LBM4a, LBM5a and LBM6a are well c oriented. Texture analysis confirms hexagonal crystalline cells and reciprocal space maps show that there is a perfect orientation of the film when compared to the substrate and that larger peaks show up with an increasing thickness. Magnetization data analysis shows that for a higher thickness Curie temperature increases. Magnetization as a function of temperature shows that ferromagnetism is still observed at or above 300K and up to 380K (LBM4a and LBM5a). Reasons for this to happen may be related to several issues: metallic residues attached to silver paint traces in the back of the substrate from the sputtering growth, contamination of the substrate, oxygen ion might not be O_3^{2-} (leading to changes in the crystalline field and the oxygen octahedra). This remaining magnetization above T_C can also lead to the idea of a second Curie temperature existing at high temperatures. If so, that would mean that the thin film is not homogeneous. Observed Curie temperatures are in the range of 210K – 240K. Electrical measurements evidence that the least thick film for this substrate, LBM5a, has a metallic to insulator behavior with a transition at $T_{MR\,(LBM5a)}^{max} = 220K$. That temperature increases with thickness, as in the case of LBM4a: $T_{MR\,(LBM4a)}^{max} = 240K$.

MgO substrate thin films have a cubic structure and XRD patterns show a single possible orientation, parallel to the substrate family of planes. Textures confirm that the film has grown perfectly according to the substrate. Reciprocal space maps lead to the conclusion that film peaks grow larger with an increasing thickness and therefore interdiffusions in the interface that alter the crystallographic quality of the film are to be expected. Magnetization as a function of field evidences a much lower ferromagnetically ordered spins at 300K. Curie temperatures are in the range of 150K-160K with the exception of LBM4a ($T_C^{LBM4c} = 200\ K$), probably because of the lower partial pressure of oxygen in the sputtering process. Also, only for this sample a magnetization value of zero is observed in the M(T) data. As in Al_2O_3 substrate thin films, a second T_C is a possibility. Resistance as a function of temperature for LBM4a shows a metallic to insulator transition at 216K. On the hand, LBM5c shows a mainly insulator behavior, although with a transition at $T_{MR\,(LBM4c)}^{max} = 140K$.

Comparing thin films for both substrates, one can conclude that structure changes with an increasing thickness. Not only that, but also that the rhomboedric structure of Al_2O_3 induces higher magnetization values as well as higher T_C (comparison to thin films grown on a cubic substrate, MgO). Although Curie temperature decreases with lower oxygen partial pressure for films with MgO substrate, that situation does not happen for Al_2O_3 substrate thin films. Moreover, a relation between thickness and T_C is not shown for this structure. On the other hand, for films with grown on MgO a relation with higher thickness can be established and this temperature either is the same or increases with thickness. It is also observed that metallic to insulator transitions temperatures seem to be dependent on the substrate, achieving higher values for LBMa.

9 Future Work

As future work further structural analysis should be carried out. Textures of LBM5a for the plane (02.4) should be repeated and the pole at $\Psi \sim 54^{\circ}$ should be more carefully studied. X-Ray photoelectron spectroscopy (XPS) measurements should be carried out with the objective of investigating possible Al atoms in the interface and consequent changes in the characteristics of the thin films. This technique, as well as energy dispersive x-ray spectroscopy (EDS), measurements should also be performed in order to obtain a composition analysis. Transmission electron microscopy (TEM) measurements should be carried out as a way to confirm the different structures, calculate the cell parameters and inhomogenities near the interface.

Regarding the magnetic characterization, residues attached to silver paint in the back of the thin films should be more carefully eliminated because of possible interference in the magnetization results and VSM measurements should be repeated, with particular interest in LBMa samples since higher values of magnetization are observed. M(T) should be performed up to higher temperatures (for example 1000K) in order to understand if a second TC is obtained at higher temperatures (if that happens, it would confirm the presence of a ferromagnetic material attached to the silver paint).

Electric measurements should be performed for all the samples and a relation with the different thicknesses should be established.

References

[1] E. Dagotto, T. Hotta, e A. Moreo, "Colossal magnetoresistant materials: the key role of phase separation," *Physics Reports*, vol. 344, pp. 1-153, 2001.

[2] M. Salamon e M. Jaime, "The physics of manganites: Structure and transport," *Reviews of Modern Physics*, vol. 73, n. 3, pp. 583-628, 2001.

[3] B. Nagabhushana, R. Sreekanth Chakradhar, K. Ramesh, V. Prasad, C. Shivakumara, e G. Chandrappa, "Magnetoresistance studies on barium doped nanocrystalline manganite," *Journal of Alloys and Compounds*, vol. 450, n. 1, pp. 364-368, Fev. 2008.

[4] Barnabe et al., "Barium-Based Manganites Ln1-xBaxMnO3 with Ln = {Pr, La}: Phase Transitions and Magnetoresistance Properties," *Chemistry of Materials*, vol. 10, n. 1, pp. 252-259, Jan. 1998.

[5] M. Dine El Hannani et al., "First-principles investigations of structural, electronic and magnetic properties of cubic LaMnO3," *Materials Science in Semiconductor Processing*, vol. 11, n. 3, pp. 81-86, 2008.

[6] C. Zener, "Interaction Between the d Shells in the Transition Metals," *Physical Review*, vol. 81, n. 3, p. 440, Fev. 1951.

[7] L. P. Gor'kov e V. Z. Kresin, "Mixed-valence manganites: fundamentals and main properties," *Physics Reports*, vol. 400, n. 3, pp. 149-208, Out. 2004.

[8] J. Zhang, H. Tanaka, T. Kanki, J. Choi, e T. Kawai, "Strain effect and the phase diagram of $La_{1-x}Ba_xMnO_3$ thin films," *Physical Review B*, vol. 64, n. 18, p. 184404, Out. 2001.

[9] P. G. M. V. L. L. Radaelli, M. [. D. C. Marezio, H. Y. Hwang, e S. W. B. L. Cheong, *Structural phase diagram of perovskite $A_{0.7}A_{0.3}MnO_3$ (A = La, Pr; A = Ca, Sr, Ba): A new Imma allotype*. 1996.

[10] A. Haghiri-Gosnet e J. Renard, "CMR manganites: physics, thin films and devices," *Journal of Physics D: Applied Physics*, vol. 36, n. 8, pp. R127-R150, 2003.

[11] C. Rao e R. Mahesh, "Giant magnetoresistance in manganese oxides," *Current Opinion in Solid State and Materials Science*, vol. 2, n. 1, pp. 32-39, Fev. 1997.

[12] B. D. Cullity e C. D. Graham, *Introduction to magnetic materials*. Wiley-IEEE, 2009.

[13] S. Chikazumi, *Physics of Ferromagnetism*, 2.º ed. Oxford University Press, 1997.

[14] K. Daoudi, M. Oueslati, T. Tsuchiya, T. Nakajima, e K. Kawaguchi, "Strain Effect on the Electrical and Magnetic Properties of La0.7Ba0.3MnO3 Thin Films Grown by Metal-Organic Deposition," *Journal of Superconductivity and Novel Magnetism*, 2010.

[15] D. Shulyatev et al., "Floating zone growth of La1-xBaxMnO3 single crystals," *Journal of Crystal Growth*, vol. 291, n. 1, pp. 262-266, Mai. 2006.

[16] A. Urushibara, Y. Moritomo, T. Arima, A. Asamitsu, G. Kido, e Y. Tokura, "Insulator-metal transition and giant magnetoresistance in $La_{1-x}Sr_xMnO_3$," *Physical Review B*, vol. 51, n. 20, p. 14103, Mai. 1995.

[17] H. Im, G. Chon, S. M. Lee, B. Koo, C. Lee, e M. Jung, "Preparation and characterization of $La_{0.7}AE_{0.3}MnO_3$ (AE=Ca, Sr, Ba): Perovskite structured manganites," *Journal of Magnetism and Magnetic Materials*, vol. 310, n. 2, pp. 2668-2670, Mar. 2007.

[18] J. J. Urban, L. Ouyang, M. Jo, D. S. Wang, e H. Park, “Synthesis of Single-Crystalline La1-xBaxMnO3 Nanocubes with Adjustable Doping Levels,” *Nano Letters*, vol. 4, n. 8, pp. 1547-1550, 2004.

[19] D. L. Smith, *Thin-Film Deposition: Principles and Pratices*. Mc Graw-Hill, 1995.

[20] K. Wasa e S. Hayakawa, *Handbook of sputter deposition technology principles, technology and applications*. Park Ridge: Noyes Publications, 1991.

[21] S. Swann, “Magnetron sputtering,” *Physics in Technology*, vol. 19, n. 2, pp. 67-75, 1988.

[22] J. G. Han, “Recent progress in thin film processing by magnetron sputtering with plasma diagnostics,” *Journal of Physics D: Applied Physics*, vol. 42, n. 4, p. 043001, 2009.

[23] B. D. Cullity, *Elements of X-Ray Diffraction*, 2.º ed. Addison-Wesley Publishing Company, Inc., 1978.

[24] P. F. Fewster, *X-ray scattering from semiconductors*. World Scientific, 2000.

[25] N. Herres, H. Obloh, K. H. Bachem, e K. Helming, “X-ray analysis of the texture of heteroepitaxial gallium nitride films,” *Materials Science and Engineering B*, vol. 59, n. 1, pp. 202-206, Mai. 1999.

[26] S. Foner, “Versatile and Sensitive Vibrating-Sample Magnetometer,” *Review of Scientific Instruments*, vol. 30, n.7, pp. 548-558, 1959.

[27] A. P. Schuetze, W. Lewis, C. Brown, e W. J. Geerts, “A laboratory on the four-point probe technique,” *American Journal of Physics*, vol. 72, n. 2, p. 149, 2004.